Title

SANISAND-MSf: a sand plasticity model with memory surface and semifluidised state

Journal

Geotechnique, 72(3)

ISSN

0016-8505 1751-7656

Authors

Yang, Ming

Taiebat, Mahdi

Dafalias, Yannis F

Publication Date

2022-03-01

DOI

10.1680/jgeot.19.P.363

Peer reviewed

Yang, M. *et al.* (2022). *Géotechnique* **72**, No. 3, 227–246 [https://doi.org/10.1680/jgeot.19.P.363]

SANISAND-MSf: a sand plasticity model with memory surface and semifluidised state

MING YANG*, MAHDI TAIEBAT† and YANNIS F. DAFALIAS‡

A new constitutive model for sand is formulated by incorporating two new constitutive ingredients into the platform of a reference critical state compatible bounding surface plasticity model with kinematic hardening, in order to address primarily the undrained cyclic response. The first ingredient is a memory surface for more precisely controlling stiffness affecting the plastic deviatoric and volumetric strains and ensuing excess pore pressure development in the pre-liquefaction stage. The second ingredient is the concept of a semifluidised state and the related formulation of stiffness and dilatancy degradation, aiming at modelling large shear strain development in the post-liquefaction stage. In parallel, a modified flow rule aimed at providing a better description of non-proportional monotonic and cyclic loading is introduced. With a single set of constants, for which a detailed calibration procedure is provided, this new model successfully simulates undrained cyclic torsional and triaxial tests with different cyclic stress ratios, separately for the pre- and post-liquefaction stages, as well as liquefaction strength curves based on r_u and shear strain criteria for initial liquefaction. The successful reproduction of the sand element response under undrained cyclic shearing contributes to future applications in realistic and thorough seismic site response analysis.

KEYWORDS: constitutive relations; liquefaction; plasticity; repeated loading; sands; stiffness; stress path

INTRODUCTION

During the dynamic analysis of geostructures, the phenomenon of sand liquefaction is a predominant event that must be accounted for. Hence, the underlying mechanism and patterns of liquefaction have been explored by laboratory experimentalists, where regular harmonic loading is usually exerted on the soil specimen. An undrained cyclic torsional test on Ottawa-F65 sand with the relative density $D_r = 60\%$ is presented in Fig. 1 to illustrate the response when the sample is sheared with cyclic stress ratio (CSR) 0·20, where CSR is the ratio of the cyclic shear stress amplitude τ^{amp} and the initial mean effective stress p_0. The stress path of shear stress τ and mean effective stress p in Fig. 1(a) and the shear stress–strain curves in Fig. 1(b) can be decomposed into two stages based on whether the mean effective stress p reaches zero or not, termed the pre- and post-liquefaction stages, respectively, with the following response characteristics: (*a*) intense plastic volumetric contraction tendencies along with small shear strain in pre-liquefaction stage; (*b*) large but limited shear deformation with increasing amplitude in the post-liquefaction stage, where the mean effective stress almost vanishes instantaneously and repeatedly, also called cyclic mobility (Castro, 1975).

Manuscript received 3 December 2019; revised manuscript accepted 25 September 2020. Published online ahead of print 5 November 2020.
Discussion on this paper closes on 1 July 2022, for further details see p. ii.
* Department of Civil Engineering, University of British Columbia, Vancouver, BC, Canada (Orcid:0000-0002-6409-3942).
† Department of Civil Engineering, University of British Columbia, Vancouver, BC, Canada (Orcid:0000-0003-2067-8161).
‡ Department of Civil and Environmental Engineering, University of California, Davis, CA, USA; Department of Mechanics, Faculty of Applied Mathematical and Physical Sciences, National Technical University of Athens, Athens, Greece; Institute of Thermomechanics, Czech Academy of Sciences, Prague, Czech Republic (Orcid:0000-0001-9690-9291).

The effort to simulate numerically the foregoing two response characteristics has led to extensive exploration in developing different constitutive models during recent decades. Within the framework of the bounding surface (BS) plasticity and hypoplasticity (Dafalias, 1986), Wang *et al.* (1990) formulated a plastic shear modulus dependence on the accumulated deviatoric plastic strain, which can effectively represent the response shown in Fig. 1. Papadimitriou *et al.* (2001), Papadimitriou & Bouckovalas (2002) and Dafalias & Manzari (2004) used a macroscopic fabric-dilatancy tensor to influence the plastic modulus and dilatancy coefficient such that large contraction occurs upon loading reversal, after a dilative phase, that brings the mean effective stress p close to zero and enables the simulation of the typical butterfly shape, as shown in Fig. 1(a). To address bounded strain cyclic mobility, Elgamal *et al.* (2003) activated a constant-volume perfectly plastic phase with the stress state frozen, when the loading stress path intersects the phase transformation line at low confinement, until a user-defined octahedral shear strain increment is accumulated. Khosravifar *et al.* (2018) updated the flow rule to address dependence on number of loading cycles, effective overburden stress and static shear stress. Boulanger & Ziotopoulou (2013) addressed the observed cyclic stiffness degradation as a function of quantities related to cumulative plastic shear strains and proposed accordingly the PM4Sand model, which is based on the Dafalias & Manzari (2004) platform. Zhang & Wang (2012) and Wang *et al.* (2014) decomposed the dilatancy and volumetric strain rate into reversible and irreversible components, introduced the concept of a volumetric strain threshold below which the soil is considered liquefied, and used cumulative irreversible volumetric strain as a model parameter. In addition, these authors were able to address the phenomenon of large but limited shear strain accumulation in the post-liquefaction stage.

These and several other similar approaches have contributed significantly to the modelling of cyclic mobility; however, they share a general shortcoming and a lack of

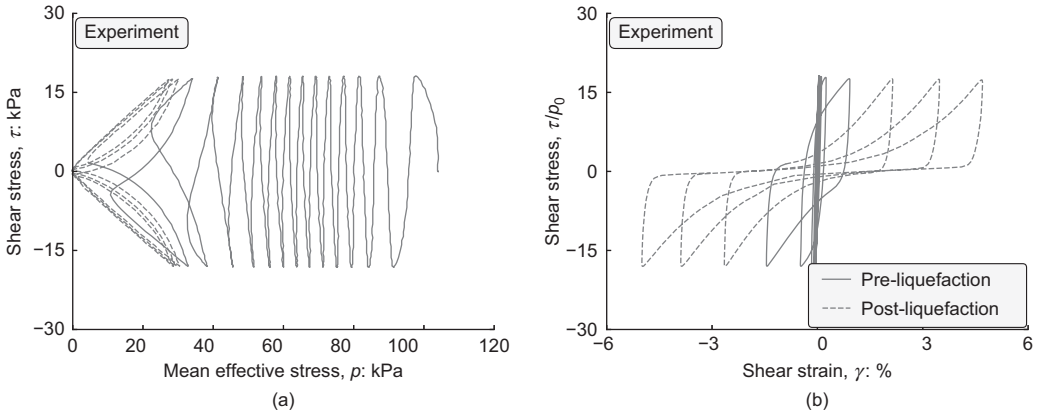

Fig. 1. Experimental data of undrained cyclic torsional test for Ottawa-F65 sand at D_r=60% after Ueda *et al.* (2018): (a) stress path; (b) stress–strain response

calibration flexibility for separate pre- and post-liquefaction response simulations. The shortcoming is the use of a quantity related to cumulative plastic volumetric or shear strain in their formulation for dilatancy determination or stiffness degradation that stays in the model after the completion of a cyclic loading process, based on the non-decreasing nature of a cumulative quantity. Yet, there is no constitutive mechanism to eliminate such quantity in subsequent drained or undrained monotonic and cyclic loading, which are thus affected unduly and irrationally by a past cyclic loading event. The lack of calibration flexibility is that while these models can fit on purpose the practically important liquefaction strength curve – that is, CSR against the total number of cycles N_{ini} for reaching the so-called initial liquefaction – such overall fitting does not necessarily correspond to correct fitting of the general stress–strain and undrained stress path response in the pre- and post-liquefaction stages separately. This is because there are no constitutive mechanisms for addressing the cyclic response separately for pre- and post-liquefaction stages.

The objective of this work is to present a new constitutive model for sands, by remedying two simulative inadequacies of a reference two-surface constitutive model by Dafalias & Manzari (2004), abbreviated as the DM04 model, which is an extension of its precursor by Manzari & Dafalias (1997). The DM04 model is critical state compatible and is built within the framework of BS plasticity; thus, by the very nature of the BS, it can address qualitatively the response under cyclic loading. However, the first simulative inadequacy is that, with stiffness determined by fitting monotonic undrained loading, it over-predicts the pore water pressure and shear strain accumulation under cyclic loading in the pre-liquefaction stage. Increasing the stiffness by means of increasing the value of the plastic modulus, K_p, will address successfully both pore water pressure and shear strain accumulation simultaneously, since both depend on plastic modulus, but at the same time it will disqualify the simulation under monotonic loading. It is therefore necessary to invent a constitutive scheme that can increase the stiffness under cyclic loading without altering the stiffness under monotonic loading.

This scheme introduces a new constitutive ingredient described by the concept and role of a 'memory surface' (MS) in stress space that stores a previously experienced range of stress ratio while increasing the stiffness for stress states within the MS without altering the stiffness for stress states on the MS during monotonic loading. Memory surfaces of various types go quite some way back in time, as in the work of Wang *et al.* (1990), Stallebrass & Taylor (1997), Maleki *et al.* (2009) and di Benedetto *et al.* (2014). The MS adopted in this study is a multifaceted modification of the original proposition by Corti *et al.* (2016) that was later adjusted by Liu *et al.* (2019) to be compatible with the DM04 model platform. The use of the MS was shown to be successful in simulating plastic volumetric and deviatoric strain variations in drained cyclic shear tests, but has not yet been tested extensively for simulations of multiple data under undrained conditions. It must be mentioned that the MS introduced by Corti *et al.* (2016) fades away during dilation, usually obtained by extensive monotonic loading of dense samples, thus returning to its original size before the cyclic loading, ready to play its role again upon a new such loading, an original feature adopted in the present work.

The second simulative inadequacy of the reference DM04 model is that after reaching the post-liquefaction stage under undrained cyclic loading, the undrained stress path stabilises, acquiring the usual butterfly shape, and similarly the cyclic stress–strain loops stabilise at a fixed shear strain amplitude. And while the butterfly stabilised shape is desirable for the undrained stress path, because it is exactly what experimental data show, the stress–strain stabilisation is against the experimental observation of increasing shear amplitude with number of post-liquefaction cycles, with an eventual saturation level. Contrary to what was done with the MS for the pre-liquefaction stage, namely to increase the stiffness by way of the plastic modulus K_p for both deviatoric and volumetric plastic strain rates, now one must progressively decrease the stiffness only for deviatoric plastic strain rate in order to achieve the increasing shear strain amplitude, while maintaining the same stiffness for plastic volumetric strain rate in order to maintain the stabilised butterfly-shaped undrained stress path. This new combination of stiffness modification protocol can be achieved by decreasing simultaneously by the same factor the plastic modulus K_p and the dilatancy D. This is because the decrease of K_p will achieve the shear strain amplitude increase, while the same decrease of D will maintain fixed the value of the ratio D/K_p on which the plastic volumetric strain rate and consequently the undrained stress path depend, thus maintaining the same butterfly shape of the latter. Notice that the foregoing conclusions are valid for any plasticity model because they address the basic constitutive relations irrespective of the specific model they are related to.

The above required constitutive modification to the DM04 model was in fact addressed in the paper by Barrero *et al.* (2020) by a new constitutive ingredient reflecting the physical existence of a 'semifluidised (Sf) state' for very low effective mean stress reached in the post-liquefaction stage. It introduced a new internal degradation variable for plastic modulus and dilatancy, named the 'strain liquefaction factor' (SLF),

that increases towards a saturation value of unity during undrained cyclic loading, while it decreases in a continuous way upon subsequent drainage. Notice that both the evolution of, and analytical effect on K_p and D by the SLF are active only for states within the semifluidised state, while leaving almost intact the response outside that state.

The introduction of the two new constitutive ingredients of MS and SLF, besides remedying the two simulative inadequacies of the DM04 model under undrained cyclic loading, also addresses the aforementioned shortcoming and lack of calibration flexibility encountered in various other constitutive models. First, the fact that the MS fades away upon dilation and the SLF demise upon drainage, allows a new cyclic loading to start anew without any unjustified effect from a previously performed cyclic loading that resulted in accumulated and permanently stored quantities such as cumulative shear strain. Second, the MS and SLF are aimed at improving the cyclic stress–strain response for pre- and post-liquefaction stages, respectively, without affecting each other; thus, they contain the seed for a separate rather than overall successful simulation of the CSR against total number of cycles in pre- and post-liquefaction stages.

The new model maintains of course all innate capabilities of the DM04 model to be critical state compatible and effective in simulating the response under various pressures and densities for monotonic loading. In fact, its capability to simulate monotonic non-proportional loading, and its control of strain accumulation shift under cyclic triaxial loading in compression and extension, are improved by two small modifications that will be described in the next section. Its effectiveness for cyclic loading will be shown by successful simulation of two extensive experimental databases on undrained cyclic torsional and triaxial tests with different CSRs. In the process, the detailed calibration procedures for the model constants related to the new constitutive ingredients, the semifluidised state and the MS, will be fully explained. These two new constitutive ingredients suggest the name SANISAND-MSf for the model, because it is a member of the SANISAND family of models (Taiebat & Dafalias, 2008), with M standing for 'memory surface' and Sf for 'semifluidised state'.

In terms of basic notation, tensor-value quantities will be shown by bold face characters and the symbol : between two tensors denotes summations over the adjacent pairs of indices in reverse order of the tensors, which in the case of second-order tensors implies the trace, namely $\mathrm{tr}(\boldsymbol{AB}) = \boldsymbol{A} : \boldsymbol{B} = A_{ij}B_{ji}$.

REFERENCE DM04 MODEL

The DM04 has four conical surfaces, as illustrated in Fig. 2 in the deviatoric stress space, shown for convenience only as the π-plane for the stress ratio. These surfaces are a small yield surface (YS) centred at the back-stress ratio $\boldsymbol{\alpha}$ that obeys kinematic hardening (KH), and three other origin-concentric surfaces: bounding surface (BS), critical state surface (CS) and dilatancy surface (DS). A mapping rule from the origin along the unit-norm deviatoric tensor $\boldsymbol{n}$, normal to the YS at the stress ratio $\boldsymbol{r}$, specify image points on the BS and DS whose distances from the current back-stress ratio $\boldsymbol{\alpha}$ control the plastic modulus and dilatancy, respectively.

The constitutive equations of the DM04 model are presented collectively in Table 1, together with some modifications to be discussed in the sequel. With more details provided in the paper by Dafalias & Manzari (2004), it is only expedient to outline briefly here the symbols and basic definitions. The elastic and plastic strains are denoted by the superscripts e and p, respectively, while a superposed

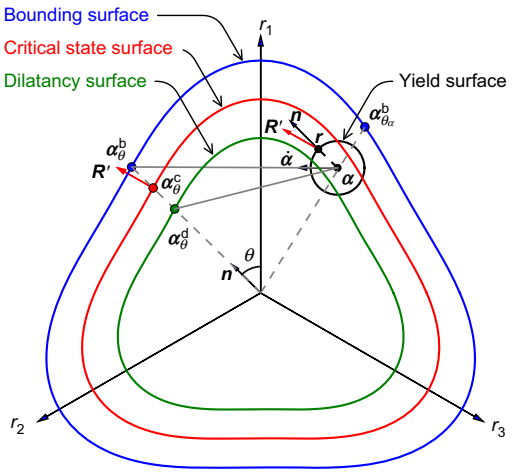

Fig. 2. Schematic illustration of model surfaces and mapping rules on the deviatoric stress ratio π plane

dot implies the rate. The $p = \mathrm{tr}(\boldsymbol{\sigma})/3$ is the mean effective stress, with $\boldsymbol{\sigma}$ being the effective stress tensor and $\mathrm{tr}(\cdot)$ the trace operator; $\boldsymbol{s} = \boldsymbol{\sigma} - p\boldsymbol{I}$ is the deviatoric stress tensor, with $\boldsymbol{I}$ being the second-order identity tensor, and $\boldsymbol{r} = \boldsymbol{s}/p$ is the stress ratio in Fig. 2; $\varepsilon_v = \mathrm{tr}(\boldsymbol{\varepsilon})$ is the volumetric strain, with $\boldsymbol{\varepsilon}$ being the strain tensor; $\boldsymbol{e} = \boldsymbol{\varepsilon} - (\varepsilon_v/3)\boldsymbol{I}$ is the deviatoric strain tensor; L is the plastic multiplier that includes the plastic modulus K_p in its denominator and is enclosed in the Macaulay brackets such that $\langle L\rangle = L$ if $L \geq 0$ and $\langle L\rangle = 0$ if $L < 0$; D is the dilatancy ratio; $\boldsymbol{R}'$ represents the deviatoric flow rule direction normal to the CS surface at the image point $\boldsymbol{\alpha}^{\mathrm{c}}_{\theta}$, also shown transferred at the stress ratio point $\boldsymbol{r}$, Fig. 2. The A_0 and h are directly related to dilatancy and plastic modulus, respectively, and their definitions are of cardinal importance for the performance of the model. The $\boldsymbol{z}$ is an evolving dilatancy fabric tensor whose role is to induce large contraction upon unloading after a dilative phase. The $\boldsymbol{\alpha}_{\mathrm{in}}$ is the initial value of $\boldsymbol{\alpha}$ at initialisation of a new loading process and is updated when the denominator of h becomes negative, as per the rules discussed by Dafalias (1986). The $g(\theta, c)$ is the interpolation function for the BS, DS and CS, with θ the Lode angle and c the ratio between triaxial extension and compression critical stress ratio values; $\psi = e - e_c$ is the state parameter (Been & Jefferies, 1985) defined as the difference between the current void ratio e and the critical void ratio e_c at the same p on the critical state line (CSL) in the e–p space (Li & Wang, 1998).

Two modifications are introduced to the DM04 model. The first defines a modified flow rule along $\boldsymbol{R}^*$ obtained by interpolation between $\boldsymbol{n}$ and the unit norm $\boldsymbol{R}'/||\boldsymbol{R}'||$, with $||.||$ being the norm operator, as

$$\boldsymbol{R}^* = I(x_\alpha)\boldsymbol{n} + [1 - I(x_\alpha)]\frac{\boldsymbol{R}'}{||\boldsymbol{R}'||} \tag{1}$$

with the interpolation factor $x_\alpha = \langle \alpha^{\mathrm{b}}_{\theta_\alpha} - ||\boldsymbol{\alpha}||\rangle / \alpha^{\mathrm{b}}_{\theta_\alpha}$ measuring the relative distance of $\boldsymbol{\alpha}$ from its BS projection $\boldsymbol{\alpha}^{\mathrm{b}}_{\theta_\alpha}$ along the radius from the origin (see Table 1 for the definition of the θ_α and the unbold $\alpha^{\mathrm{b}}_{\theta_\alpha}$ that is the length of the $\boldsymbol{\alpha}^{\mathrm{b}}_{\theta_\alpha}$ shown in Fig. 2); the $I(x_\alpha)$ is an interpolation function varying together with x_α from 1 to 0, as $\boldsymbol{\alpha}$ moves from the origin onto or outside the BS, and accordingly the $\boldsymbol{R}^*$ varies from $\boldsymbol{n}$ to $\boldsymbol{R}'/||\boldsymbol{R}'||$. The choice $I(x_\alpha) = x_\alpha^2$ is made for simplicity here, as shown in the third column of Table 1, without adding a new constant (the exponent 2 is a default value). Alternative choices are possible, as for example one variant of the sigmoidal function widely used in machine learning $\sigma(x_\alpha) = I(x_\alpha) = 1/\{1 + \exp\ [-k(x_\alpha - R_c)]\}$ that approaches 1 and 0

Table 1. Changes from basic to modified DM04 model equations related to flow rule and dilatancy updates

Description	DM04 equations	Modified equations	Constants
Elastic relations	$\dot{\varepsilon}_{\mathrm{v}}^{\mathrm{e}} = \dot{p}/K;\ \ \dot{\boldsymbol{e}}^{\mathrm{e}} = \dot{\boldsymbol{s}}/(2G)$		
Plastic relations	$\dot{\varepsilon}_{\mathrm{v}}^{\mathrm{p}} = \langle L\rangle D;\ \dot{\boldsymbol{e}}^{\mathrm{p}} = \langle L\rangle \boldsymbol{R}'$	$\dot{\boldsymbol{e}}^{\mathrm{p}} = \langle L\rangle \boldsymbol{R}^{*}$	
Hypoelastic moduli	$G = G_0 p_{\mathrm{at}}(2{\cdot}97 - e)^2/(1+e)(p/p_{\mathrm{at}})^{1/2}$		G_0
	$K = 2(1+\nu)G/[3(1-2\nu)]$		ν
Yield surface	$f = \sqrt{(\boldsymbol{s} - p\boldsymbol{\alpha}) : (\boldsymbol{s} - p\boldsymbol{\alpha})} - \sqrt{2/3}pm = 0$		m
Dilatancy	$D = A_0(1 + \langle \boldsymbol{z} : \boldsymbol{n}\rangle)(\boldsymbol{\alpha}_\theta^{\mathrm{d}} - \boldsymbol{\alpha}) : \boldsymbol{n}$	$D = A_0 g(\theta, c)^{-n_g}(1 + \langle \boldsymbol{z} : \boldsymbol{n}\rangle)(\boldsymbol{\alpha}_\theta^{\mathrm{d}} - \boldsymbol{\alpha}) : \boldsymbol{n}$	A_0, n_g
Deviatoric flow rule	$\boldsymbol{R}' = B\boldsymbol{n} - C[\boldsymbol{n}^2 - (1/3)\boldsymbol{I}]$	$\boldsymbol{R}^{*} = x_\alpha^2 \boldsymbol{n} + (1 - x_\alpha^2)\boldsymbol{R}'/\|\boldsymbol{R}'\|$	
	$\boldsymbol{n} = (\boldsymbol{r} - \boldsymbol{\alpha})/\|\boldsymbol{r} - \boldsymbol{\alpha}\|$	$x_\alpha = \left\langle \alpha_{\theta_\alpha}^{\mathrm{b}} - \|\boldsymbol{\alpha}\| \right\rangle / \alpha_{\theta_\alpha}^{\mathrm{b}}$	
	$B = 1 + 3(1-c)/(2c)g(\theta, c)\cos\ 3\theta$	$\alpha_{\theta_\alpha}^{\mathrm{b}} = \sqrt{2/3}[g(\theta_\alpha, c)M\exp\ (-n^{\mathrm{b}}\psi) - m]$	c
	$C = 3\sqrt{3/2}(1-c)g(\theta, c)/c$	$\cos\ 3\theta_\alpha = \sqrt{6}\mathrm{tr}(\boldsymbol{n}_\alpha^3);\ \boldsymbol{n}_\alpha = \boldsymbol{\alpha}/\|\boldsymbol{\alpha}\|$	
	$g(\theta, c) = 2c/[(1+c) - (1-c)\cos\ 3\theta]$		
Kinematic hardening	$\dot{\boldsymbol{\alpha}} = \langle L\rangle (2/3)h(\boldsymbol{\alpha}_\theta^{\mathrm{b}} - \boldsymbol{\alpha})$		
Fabric-dilatancy rate	$\dot{\boldsymbol{z}} = -c_z\langle -\dot{\varepsilon}_{\mathrm{v}}^{\mathrm{p}}\rangle(z_{\max}\boldsymbol{n} + \boldsymbol{z})$		c_z, $z_{\max}$
Hardening coefficient	$h = b_0/[(\boldsymbol{\alpha} - \boldsymbol{\alpha}_{\mathrm{in}}) : \boldsymbol{n}]$		
	$b_0 = G_0 h_0(1 - c_h e)(p/p_{\mathrm{at}})^{-1/2}$	$b_0 = G_0 h_0 g(\theta, c)^{-n_g}(1 - c_h e)(p/p_{\mathrm{at}})^{-1/2}$	h_0, c_h
Image point on DS	$\boldsymbol{\alpha}_\theta^{\mathrm{d}} = \sqrt{2/3}[g(\theta, c)M\exp\ (n^{\mathrm{d}}\psi) - m]\boldsymbol{n}$		n^{d}, M
Image point on BS	$\boldsymbol{\alpha}_\theta^{\mathrm{b}} = \sqrt{2/3}[g(\theta, c)M\exp\ (-n^{\mathrm{b}}\psi) - m]\boldsymbol{n}$		n^{b}
Critical state line	$e_{\mathrm{c}} = e_{\mathrm{c}}^{\mathrm{ref}} - \lambda_{\mathrm{c}}(p/p_{\mathrm{at}})^{\xi}$		$e_{\mathrm{c}}^{\mathrm{ref}}$, λ_{c}, ξ

as closely as desired by the specification of its two constants k and R_{c}. Fig. 3 shows the simulation compared against data for the undrained simple shear test of Toyoura sand (data from Yoshimine *et al*. (1998), also appeared in figure 12 of the paper by Dafalias & Manzari (2004)) using four different flow rules associated with $\boldsymbol{n}$, $\boldsymbol{R}'$ and two $\boldsymbol{R}^{*}$ according to equation (1) with the aforementioned two interpolation functions. The plots in Figs 3(a) and 3(b) do not differ significantly, but the one in Fig. 3(c) shows the advantages of using the modified flow rule for non-proportional loading.

The second modification consists of dividing dilatancy D and plastic modulus K_{p} by $g(\theta, c)^{n_g}$, with n_g a model constant, as shown in the third column of Table 1; the foregoing division of K_{p} is achieved by dividing the b_0 term of its coefficient h. Dividing both D and K_{p} by the same factor, the function of the Lode angle θ, maintains the same plastic volumetric strain rate and correspondingly pore water pressure rate and undrained stress paths, while balancing the relative magnitude of shear strain amplitude in triaxial compression and extension, thereby allowing, by a proper choice of n_g, control of the shifting of the stress–strain loops during cyclic triaxial loading. The use of $g(\theta, c)^{n_g}$ has a small effect on the stress–strain curve in extension, while the response in compression is unaltered because $g(\theta, c)^{n_g} = 1$.

MEMORY SURFACE

The MS by Corti *et al*. (2016), and its extension by Liu *et al*. (2019), is equipped with both isotropic hardening (IH) and kinematic hardening (KH) in the deviatoric stress ratio space, and its role is that of an auxiliary BS aimed at adding extra stiffness to the deviatoric and volumetric plastic strain rates for stress points within the MS, prompted by comparison of simulations with data. It is thought that the role of the MS as a stiffening constitutive ingredient is related to adjustments to the micromechanical fabric characteristics due to experienced past loading range in stress space.

The formulation of the MS developed in this study is different from that of Corti *et al*. (2016) and Liu *et al*. (2019) in regard to the following aspects.

- It is a MS for the back-stress ratio rather than the stress ratio, compatible with the formulation of DM04 model, which allows the minimum of its size to be zero.
- It derives the evolution of MS in general, using BS techniques, as opposed to the assumption that the virgin loading formulation is extended to cases under general loading (Liu *et al*., 2019).
- It tackles the singular case where a denominator can go to zero under certain loading conditions, existing in Liu *et al*. (2019).
- It does not make use of MS for the determination of dilatancy D that is evaluated with the equation listed in Table 1 using the dilatancy fabric tensor $\boldsymbol{z}$, according to the DM04 model. If an improvement of dilatancy is found necessary, one could make use of the dilatancy-triggering surface proposed by Woo *et al*. (2019) in a role similar to that of the MS while being compatible with the DM04 model platform.

The MS is defined analytically by

$$f^{\mathrm{M}} = \sqrt{(\boldsymbol{\alpha}_\theta^{\mathrm{M}} - \boldsymbol{\alpha}^{\mathrm{M}}) : (\boldsymbol{\alpha}_\theta^{\mathrm{M}} - \boldsymbol{\alpha}^{\mathrm{M}})} - \sqrt{2/3}m^{\mathrm{M}} = 0 \qquad (2)$$

where $\boldsymbol{\alpha}^{\mathrm{M}}$ is its centre and m^{M} its size. As illustrated in Fig. 4, $\boldsymbol{\alpha}_\theta^{\mathrm{M}}$ is the image point of $\boldsymbol{\alpha}$ on the MS obtained by projection from $\boldsymbol{\alpha}^{\mathrm{M}}$ along $\boldsymbol{n}$ on it, expressed analytically by

$$\boldsymbol{\alpha}_\theta^{\mathrm{M}} = \boldsymbol{\alpha}^{\mathrm{M}} + \sqrt{\frac{2}{3}}m^{\mathrm{M}}\boldsymbol{n} \qquad (3)$$

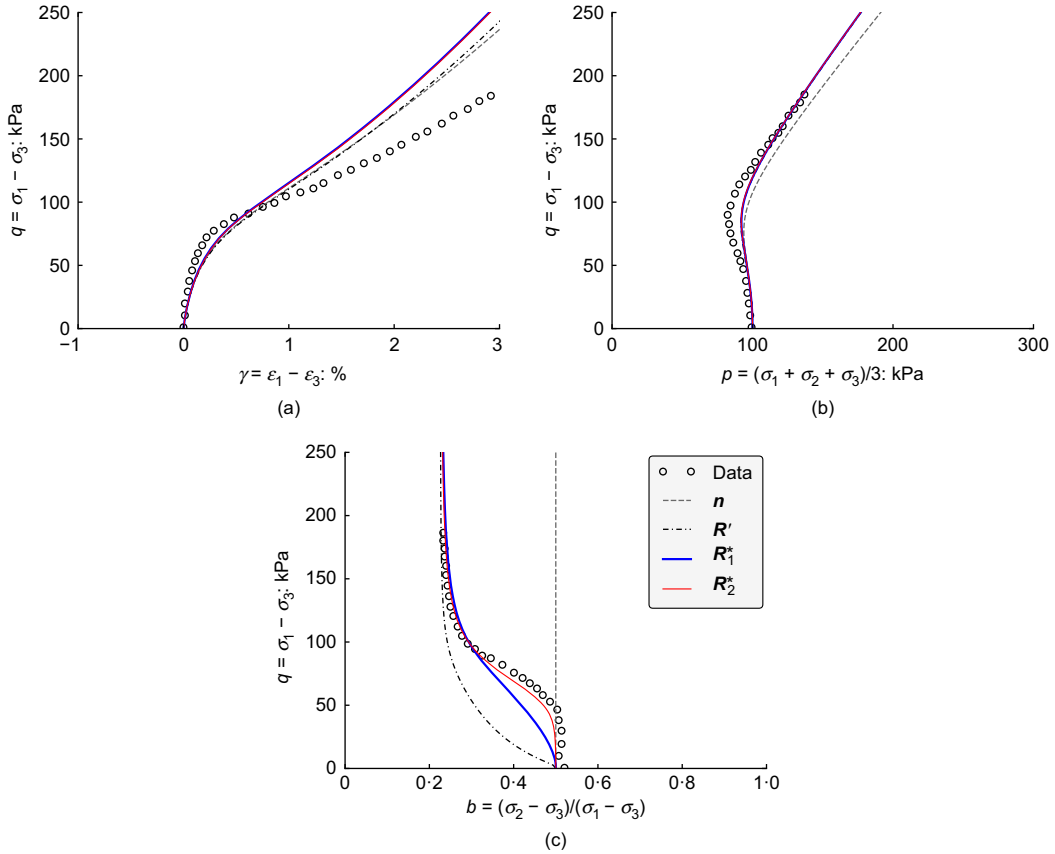

Fig. 3. Simulation of undrained simple shear test data of Toyoura sand (Yoshimine *et al.*, 1998) using flow rules associated with $\boldsymbol{n}$, $\boldsymbol{R}'$ and from equation (1) $\boldsymbol{R}_1^*$ for $\boldsymbol{l}(x_\alpha) = x_{\boldsymbol{\alpha}}^2$ and $\boldsymbol{R}_2^*$ for $\boldsymbol{l}(x_{\boldsymbol{\alpha}}) = \boldsymbol{\sigma}(x_{\boldsymbol{\alpha}})$ where $\boldsymbol{k} = 15$ and $R_c = 0{\cdot}6$

where the use of the subscript θ in all the above is indicative of the corresponding Lode angle θ. The distance of $\boldsymbol{\alpha}$ from $\boldsymbol{\alpha}_\theta^{\mathrm{M}}$ projected on $\boldsymbol{n}$ will be the key new quantity for increasing the stiffness. During the loading process one must make sure that the $\boldsymbol{\alpha}$ does not move outside the MS so that the aforementioned quantity remains positive. To this extent, one can write

$$\begin{aligned}\dot{\boldsymbol{\alpha}} &= \dot{\boldsymbol{\alpha}}_\theta^{\mathrm{M}} + \langle L\rangle \frac{2}{3} h^* \left(\boldsymbol{\alpha}_\theta^{\mathrm{M}} - \boldsymbol{\alpha}\right) \\ &= \dot{\boldsymbol{\alpha}}^{\mathrm{M}} + \sqrt{\frac{2}{3}} \dot{m}^{\mathrm{M}} \boldsymbol{n} + \sqrt{\frac{2}{3}} m^{\mathrm{M}} \dot{\boldsymbol{n}} + \langle L\rangle \frac{2}{3} h^* \left(\boldsymbol{\alpha}_\theta^{\mathrm{M}} - \boldsymbol{\alpha}\right)\end{aligned} \tag{4}$$

where the rate of equation (3) was used in deriving equation (4), which is valid for $\boldsymbol{\alpha}$ inside or on the MS. Equation (4) simply states that $\boldsymbol{\alpha}$ will move as much as its image point $\boldsymbol{\alpha}_\theta^{\mathrm{M}}$ plus an additional motion along $\boldsymbol{\alpha}_\theta^{\mathrm{M}} - \boldsymbol{\alpha}$ controlled by a free to choose modulus h^*, hence guaranteeing that $\boldsymbol{\alpha}$ will never cross and move outside the MS because the additional motion will stop when $\boldsymbol{\alpha}_\theta^{\mathrm{M}} - \boldsymbol{\alpha} = \boldsymbol{0}$ no matter what the value of h^* is. By multiplying equation (4) with $\boldsymbol{n}$ and taking the trace of each term, one obtains

$$\dot{\boldsymbol{\alpha}} : \boldsymbol{n} = \dot{\boldsymbol{\alpha}}^{\mathrm{M}} : \boldsymbol{n} + \sqrt{\frac{2}{3}} \dot{m}^{\mathrm{M}} + \langle L\rangle \frac{2}{3} h^* \left(\boldsymbol{\alpha}_\theta^{\mathrm{M}} - \boldsymbol{\alpha}\right) : \boldsymbol{n} \tag{5}$$

noticing that $\dot{\boldsymbol{n}} : \boldsymbol{n} = 0$ implied by $\boldsymbol{n} : \boldsymbol{n} = 1$. Equation (5) becomes the consistency condition for the MS when $\boldsymbol{\alpha}$ is on it – that is, when $\boldsymbol{\alpha}_\theta^{\mathrm{M}} - \boldsymbol{\alpha} = \boldsymbol{0}$, as can be seen by taking the rate of f^{M} in equation (2) and observing from Fig. 4 that the normal $\boldsymbol{n}$ to the YS at $\boldsymbol{r}$ is the same as the normal $\boldsymbol{n}$ to the MS at $\boldsymbol{\alpha}_\theta^{\mathrm{M}}$.

Rate of $\boldsymbol{\alpha}^{\mathrm{M}}$

Referring to Fig. 4 one can observe that eventually $\boldsymbol{\alpha}$ will reach the BS at its image point $\boldsymbol{\alpha}_\theta^{\mathrm{b}}$, as per the corresponding rate equation for $\boldsymbol{\alpha}$ in Table 1, and the MS at its image point $\boldsymbol{\alpha}_\theta^{\mathrm{M}}$; thus, $\boldsymbol{\alpha}_\theta^{\mathrm{M}}$ will reach the BS at the same point $\boldsymbol{\alpha}_\theta^{\mathrm{b}}$. Consequently the $\boldsymbol{\alpha}^{\mathrm{M}}$ will reach a point $\boldsymbol{\alpha}_\theta^{\mathrm{bM}}$, which is inwards from $\boldsymbol{\alpha}_\theta^{\mathrm{b}}$ along $\boldsymbol{n}$ and defined by

$$\boldsymbol{\alpha}_\theta^{\mathrm{bM}} = \boldsymbol{\alpha}_\theta^{\mathrm{b}} - \sqrt{\frac{2}{3}} m^{\mathrm{M}} \boldsymbol{n} \tag{6}$$

Based on equations (3) and (6) one has $\boldsymbol{\alpha}_\theta^{\mathrm{bM}} - \boldsymbol{\alpha}^{\mathrm{M}} = \boldsymbol{\alpha}_\theta^{\mathrm{b}} - \sqrt{2/3} m^{\mathrm{M}} \boldsymbol{n} - \boldsymbol{\alpha}^{\mathrm{M}} = \boldsymbol{\alpha}_\theta^{\mathrm{b}} - \boldsymbol{\alpha}_\theta^{\mathrm{M}}$; thus, the following rate

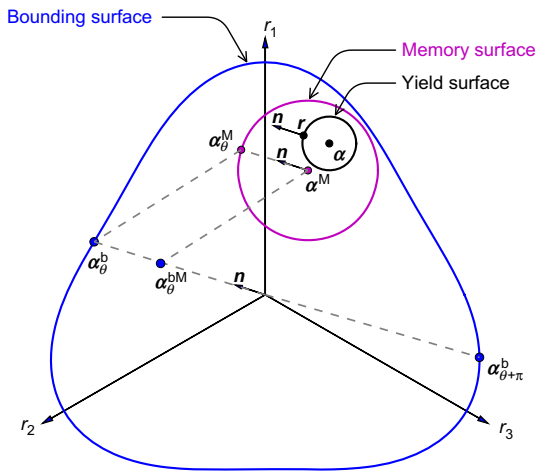

Fig. 4. Illustration of the conceptual framework of bounding-memory surface models

equation of evolution can be written for $\boldsymbol{\alpha}^{\mathrm{M}}$– that is, the KH of the MS

$$\dot{\boldsymbol{\alpha}}^{\mathrm{M}} = \langle L\rangle \frac{2}{3} h^{\mathrm{M}} \left(\boldsymbol{\alpha}_{\theta}^{\mathrm{bM}} - \boldsymbol{\alpha}^{\mathrm{M}}\right) = \langle L\rangle \frac{2}{3} h^{\mathrm{M}} \left(\boldsymbol{\alpha}_{\theta}^{\mathrm{b}} - \boldsymbol{\alpha}_{\theta}^{\mathrm{M}}\right) \tag{7}$$

with h^{M} an appropriate modulus to be defined in the following.

Rate of m^{M}

The isotropic hardening/softening (IH) of the MS is given by the rate of its size m^{M}. A modification of the proposition by Liu *et al.* (2019) can be expressed by

$$\dot{m}^{\mathrm{M}} = \sqrt{\frac{3}{2}} \dot{\boldsymbol{\alpha}}^{\mathrm{M}} : \boldsymbol{n} - \frac{m^{\mathrm{M}}}{\varsigma} \langle -\dot{\varepsilon}_{\mathrm{v}}^{\mathrm{p}} \rangle \tag{8}$$

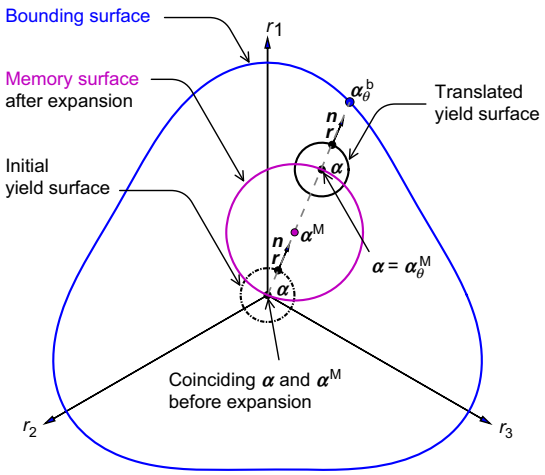

Fig. 5. Memory surface expansion and translation during virgin loading

Observe the deletion from the second term of equation (8), of the complicated term f_{shr} used in the corresponding equation (16) of the proposition by Liu *et al.* (2019), which is necessary to keep the MS from becoming smaller than the YS. This is because in the present case the MS refers to the back-stress ratio $\boldsymbol{\alpha}$ and not to the stress ratio $\boldsymbol{r}$, hence, it is allowed to shrink down to zero size – that is, $m^{\mathrm{M}} = 0$ – due to dilation. The MS shrinking was an original suggestion by Corti *et al.* (2016) that is very important because it provides the mechanism to eliminate a previous MS upon dilation and start anew in a subsequent loading process.

The next step would be to substitute the expression of $\dot{\boldsymbol{\alpha}}$ as listed in Table 1, and equations (7) and (8) into the consistency equation (5) and solve for the parameter h^{M} necessary for the operation of equation (7). In doing so, two traps may arise. First, during dilation and softening, which is common to dense sands, the second term of the right-hand side (RHS) of equation (8) may render the size m^{M} of the MS zero, and if the first term is negative, then equation (8) will yield an unacceptable negative value of m^{M}. This eventuality is possible because one may have $\boldsymbol{\alpha} = \boldsymbol{\alpha}_{\theta}^{\mathrm{M}}$ during monotonic loading from the origin for which all tensors are along $\boldsymbol{n}$, and because during softening the $\boldsymbol{\alpha}$ is outside the BS, a standard feature of the DM04 model, the $\boldsymbol{\alpha}_{\theta}^{\mathrm{M}}$ will be as well; consequently, it follows from equation (7) that the $\dot{\boldsymbol{\alpha}}^{\mathrm{M}}$, which is along $\boldsymbol{\alpha}_{\theta}^{\mathrm{b}} - \boldsymbol{\alpha}_{\theta}^{\mathrm{M}}$, will be along $-\boldsymbol{n}$ (recall the $\boldsymbol{\alpha}_{\theta}^{\mathrm{M}}$ is further out than $\boldsymbol{\alpha}_{\theta}^{\mathrm{b}}$ along $\boldsymbol{n}$); hence, the first term of the RHS of equation (8) will be negative, establishing the first trap. The second trap is more serious. In solving equation (5) for h^{M}, after the aforementioned substitutions, the term $\left(\boldsymbol{\alpha}_{\theta}^{\mathrm{b}} - \boldsymbol{\alpha}_{\theta}^{\mathrm{M}}\right) : \boldsymbol{n}$ will appear in the denominator and it is possible for cases where some part of the MS has moved outside the BS to have $\left(\boldsymbol{\alpha}_{\theta}^{\mathrm{b}} - \boldsymbol{\alpha}_{\theta}^{\mathrm{M}}\right) : \boldsymbol{n} = 0$ even if $\boldsymbol{\alpha}_{\theta}^{\mathrm{b}} \neq \boldsymbol{\alpha}_{\theta}^{\mathrm{M}}$. This will cause singularity and an infinite value for h^{M} that may create serious numerical problems upon implementation. Such zeroing of the corresponding quantity $(\boldsymbol{r}_{\theta}^{\mathrm{b}} - \boldsymbol{r}^{\mathrm{M}}) : \boldsymbol{n}$ may occur in the

Table 2. Changes from modified DM04 to SANISAND-MSf model equations related to memory surface and semifluidised state

Description	DM04 modified equations	SANISAND-MSf	Constants*
Memory surface	—	$f^{\mathrm{M}} = \sqrt{\left(\boldsymbol{\alpha}_{\theta}^{\mathrm{M}} - \boldsymbol{\alpha}^{\mathrm{M}}\right) : \left(\boldsymbol{\alpha}_{\theta}^{\mathrm{M}} - \boldsymbol{\alpha}^{\mathrm{M}}\right)} - \sqrt{2/3} m^{\mathrm{M}} = 0$	
Image point on MS	—	$\boldsymbol{\alpha}_{\theta}^{\mathrm{M}} = \boldsymbol{\alpha}^{\mathrm{M}} + \sqrt{2/3} m^{\mathrm{M}} \boldsymbol{n}$	
		$\dot{\boldsymbol{\alpha}}^{\mathrm{M}} = \langle L\rangle (2/3) h^{\mathrm{M}} \left(\boldsymbol{\alpha}_{\theta}^{\mathrm{b}} - \boldsymbol{\alpha}_{\theta}^{\mathrm{M}}\right)$	
		$\dot{m}^{\mathrm{M}} = \langle L\rangle [\sqrt{2/3} c_{\mathrm{c}} h^{\mathrm{M}} \langle \left(\boldsymbol{\alpha}_{\theta}^{\mathrm{b}} - \boldsymbol{\alpha}_{\theta}^{\mathrm{M}}\right) : \boldsymbol{n}\rangle - m^{\mathrm{M}}/\varsigma \left|\left(\boldsymbol{\alpha}_{\theta}^{\mathrm{b}} - \boldsymbol{\alpha}_{\theta}^{\mathrm{M}}\right) : \boldsymbol{n}\right| \langle -D\rangle]$	$c_{\mathrm{c}} = 1$ $\varsigma = 0{\cdot}00001$
		$h^{\mathrm{M}} = \left\{h + \sqrt{3/2} \left(m^{\mathrm{M}}/\varsigma\right) \mathrm{sgn}\left[\left(\boldsymbol{\alpha}_{\theta}^{\mathrm{b}} - \boldsymbol{\alpha}_{\theta}^{\mathrm{M}}\right) : \boldsymbol{n}\right] \langle -D\rangle\right\} / \left\{1 + c_{\mathrm{c}} \mathcal{H}\left[\left(\boldsymbol{\alpha}_{\theta}^{\mathrm{b}} - \boldsymbol{\alpha}_{\theta}^{\mathrm{M}}\right) : \boldsymbol{n}\right]\right\}$	
Hardening coefficient	$h = b_0/[(\boldsymbol{\alpha} - \boldsymbol{\alpha}_{\mathrm{in}}) : \boldsymbol{n}]$	$h = \{b_0/[(\boldsymbol{\alpha} - \boldsymbol{\alpha}_{\mathrm{in}}) : \boldsymbol{n}]\} \times \exp\{[\mu_0/(\|\boldsymbol{\alpha}_{\mathrm{in}}\|^u + \varepsilon)] (b^{\mathrm{M}}/b_{\mathrm{ref}})^w\}$	μ_0, u $\varepsilon = 0{\cdot}01$, $w = 2$
		$b^{\mathrm{M}} = \left(\boldsymbol{\alpha}_{\theta}^{\mathrm{M}} - \boldsymbol{\alpha}\right) : \boldsymbol{n}$	
		$b_{\mathrm{ref}} = \left(\boldsymbol{\alpha}_{\theta}^{\mathrm{b}} - \boldsymbol{\alpha}_{\theta+\pi}^{\mathrm{b}}\right) : \boldsymbol{n}$	
SLF rate	—	$\dot{\ell} = \langle L\rangle [c_{\ell} \langle 1 - p_{\mathrm{r}}\rangle (1 - \ell)^{n_{\ell}}] - c_{\mathrm{r}} \ell |\dot{\varepsilon}_{\mathrm{v}}|$	c_{ℓ}, $n_{\ell} = 8$, c_{r}
		$p_{\mathrm{r}} = p/p_{\mathrm{th}}$	$p_{\mathrm{th}} = 10\,\mathrm{kPa}$
	h_0	$h_0 = h_0' \left[\left(1 - \langle 1 - p_{\mathrm{r}}\rangle\right)^{x\ell} + f_{\ell}\right]$	x, $f_{\ell} = 0{\cdot}01$
	A_0	$A_0 = A_0' \left[\left(1 - \langle 1 - p_{\mathrm{r}}\rangle\right)^{x\ell} + f_{\ell}\right]$	

*Some constants have indicated default numerical values.

denominator of the second term of the RHS of equation (18) in the paper by Liu *et al.* (2019).

In order to avoid the foregoing two traps, the following equation is proposed in lieu of equation (8), using the plastic volumetric strain rate as given in Table 1 and equation (7)

$$\dot{m}^{\mathrm{M}} = \langle L \rangle \left[\sqrt{\frac{2}{3}} c_{\mathrm{c}} h^{\mathrm{M}} \left\langle \left(\boldsymbol{\alpha}_{\theta}^{\mathrm{b}} - \boldsymbol{\alpha}_{\theta}^{\mathrm{M}} \right) : \boldsymbol{n} \right\rangle - \frac{m^{\mathrm{M}}}{\varsigma} \left| \left(\boldsymbol{\alpha}_{\theta}^{\mathrm{b}} - \boldsymbol{\alpha}_{\theta}^{\mathrm{M}} \right) : \boldsymbol{n} \right| \langle -D \rangle \right] \tag{9}$$

One can identify the following changes in regard to equation (8). First the Macaulay brackets appear in the first term of the RHS of equation (9) by applying them to $\dot{\boldsymbol{\alpha}}^{\mathrm{M}} : \boldsymbol{n}$ and using equation (7), while treating h^{M} as positive, a hypothesis that must be confirmed at the end. Therefore, the first term will not contribute to the shrinkage of the MS when $\left(\boldsymbol{\alpha}_{\theta}^{\mathrm{b}} - \boldsymbol{\alpha}_{\theta}^{\mathrm{M}} \right) : \boldsymbol{n} < 0$, so that it excludes the aforementioned first trap of m^{M} becoming negative. Second, the quantity $\left| \left(\boldsymbol{\alpha}_{\theta}^{\mathrm{b}} - \boldsymbol{\alpha}_{\theta}^{\mathrm{M}} \right) : \boldsymbol{n} \right|$ is introduced in the second term of the RHS in order to address the eventuality of $\left(\boldsymbol{\alpha}_{\theta}^{\mathrm{b}} - \boldsymbol{\alpha}_{\theta}^{\mathrm{M}} \right) : \boldsymbol{n} = 0$ in the denominator of the solution of equation (5) for h^{M}, with which it will be cancelled. Use of an absolute value $|\cdot|$ is necessary in the case of a MS larger than the BS where the negative value of $\left(\boldsymbol{\alpha}_{\theta}^{\mathrm{b}} - \boldsymbol{\alpha}_{\theta}^{\mathrm{M}} \right) : \boldsymbol{n}$ would induce increase rather than decrease of the MS size during dilation. The factor c_{c} is added simply to provide a greater flexibility in the relative contribution of IH and KH to the evolution of m^{M}. Its default value $c_{\mathrm{c}} = 1$, proposed in Corti *et al.* (2016), implies that the rate of IH is exactly equal to the rate of KH when $\boldsymbol{\alpha}$ is on the MS; in practical terms it means that, as the $\boldsymbol{\alpha}$ moves away from the origin during virgin loading, the centre $\boldsymbol{\alpha}^{\mathrm{M}}$ of the MS is half the value of $\boldsymbol{\alpha}$ and equals m^{M}. So, the MS develops with one end on $\boldsymbol{\alpha}$ and the other fixed at the origin, as presented in Fig. 5. If $c_{\mathrm{c}} > 1$ the KH will contribute more to IH and the stress origin will be inside the MS, while if $c_{\mathrm{c}} < 1$ the KH will have a lesser contribution to IH and the origin will be left outside the MS, during virgin loading. Irrespective of the value of c_{c}, the structure of equations (7) and (9) implies that for monotonic radial virgin loading from the origin, the current back-stress ratio point will be simultaneously on the yield and memory surfaces; thus the value of c_{c} will affect the response only upon reverse loading after monotonic, as per the foregoing description of the stress origin position in relation to the MS. The constant ς, appearing in equation (9), controls the pace of MS shrinking during dilation; hence, it affects the post-liquefaction stress path. A default value of $\varsigma = 0{\cdot}00001$ is found to be effective. Finally, the assumption $h^* = h$ in equation (5) is necessary, without any significant loss of generality, for the elimination of the effect of zero denominator when $\left(\boldsymbol{\alpha}_{\theta}^{\mathrm{b}} - \boldsymbol{\alpha}_{\theta}^{\mathrm{M}} \right) : \boldsymbol{n} = 0$ because the choice $h^* = h$ makes the foregoing zero term appear also in the numerator; hence, it will be cancelled.

Based on the foregoing, substitution of $\dot{\boldsymbol{\alpha}}$ from Table 1 and equations (7) and (9) in equation (5), yields for h^{M} the solution

$$h^{\mathrm{M}} = \frac{1}{1 + c_{\mathrm{c}} \mathcal{H}\left[\left(\boldsymbol{\alpha}_{\theta}^{b} - \boldsymbol{\alpha}_{\theta}^{\mathrm{M}} \right) : \boldsymbol{n} \right]} \left\{ h + \sqrt{\frac{3}{2}} \frac{m^{\mathrm{M}}}{\varsigma} \mathrm{sgn}\left[\left(\boldsymbol{\alpha}_{\theta}^{\mathrm{b}} - \boldsymbol{\alpha}_{\theta}^{\mathrm{M}} \right) : \boldsymbol{n} \right] \langle -D \rangle \right\} \tag{10}$$

where the Heaviside function $\mathcal{H}[x] = 1$ if $x \geq 0$ and $\mathcal{H}[x] = 0$ if $x < 0$; the sign function $\mathrm{sgn}[x] = 1$ if $x > 0$, $\mathrm{sgn}[x] = 0$ if $x = 0$ and $\mathrm{sgn}[x] = -1$ if $x < 0$. Recall that in writing equation (9) it is hypothesised that $h^{\mathrm{M}} > 0$ so that it is taken outside the $\langle \cdot \rangle$ and this hypothesis must now be confirmed. Indeed when $\left(\boldsymbol{\alpha}_{\theta}^{\mathrm{b}} - \boldsymbol{\alpha}_{\theta}^{\mathrm{M}} \right) : \boldsymbol{n} > 0$ equation (10) yields $h^{\mathrm{M}} > 0$, but when $\left(\boldsymbol{\alpha}_{\theta}^{\mathrm{b}} - \boldsymbol{\alpha}_{\theta}^{\mathrm{M}} \right) : \boldsymbol{n} < 0$ it is possible to have $h^{\mathrm{M}} < 0$ depending on the relative values of the first and second terms of the RHS of equation (10). But in this case the first term of the RHS of equation (9) goes to zero anyway, irrespective of the sign of h^{M}, and any negative value of the latter has no adverse effect on the formulation for the rate of m^{M}.

The Heaviside and sign functions in equation (10) are discontinuous upon change of sign of their argument. This has no effect in radial loading if the change of sign of $\left(\boldsymbol{\alpha}_{\theta}^{\mathrm{b}} - \boldsymbol{\alpha}_{\theta}^{\mathrm{M}} \right) : \boldsymbol{n}$ occurs when $\boldsymbol{\alpha}_{\theta}^{\mathrm{b}} = \boldsymbol{\alpha}_{\theta}^{\mathrm{M}}$ because then $\dot{\boldsymbol{\alpha}}^{\mathrm{M}} = \boldsymbol{0}$; but if it happens that for a continuously changing direction $\boldsymbol{n}$ the sign of $\left(\boldsymbol{\alpha}_{\theta}^{\mathrm{b}} - \boldsymbol{\alpha}_{\theta}^{\mathrm{M}} \right) : \boldsymbol{n}$ changes without having $\boldsymbol{\alpha}_{\theta}^{\mathrm{b}} = \boldsymbol{\alpha}_{\theta}^{\mathrm{M}}$, then discontinuities in the value of h^{M} appear. However, this will show no discontinuous stress–strain response because it will only affect the rate of evolution of MS without any discontinuity of the MS itself.

The role of MS

With equations (7), (9) and (10) the evolution of the MS is complete. Its link to the DM04 model can then be expressed by modifying the value of the hardening coefficient h, listed in Table 1, as follows

$$h = \frac{b_0}{(\boldsymbol{\alpha} - \boldsymbol{\alpha}_{\mathrm{in}}) : \boldsymbol{n}} \exp\left[\frac{\mu_0}{||\boldsymbol{\alpha}_{\mathrm{in}}||^u + \varepsilon} \left(\frac{b^{\mathrm{M}}}{b_{\mathrm{ref}}} \right)^w \right] \tag{11}$$

where $b^{\mathrm{M}} = \left(\boldsymbol{\alpha}_{\theta}^{\mathrm{M}} - \boldsymbol{\alpha} \right) : \boldsymbol{n}$ and $b_{\mathrm{ref}} = \left(\boldsymbol{\alpha}_{\theta}^{\mathrm{b}} - \boldsymbol{\alpha}_{\theta+\pi}^{\mathrm{b}} \right) : \boldsymbol{n}$ (refer to Fig. 4 for identification of the foregoing tensors); $\boldsymbol{\alpha}_{\mathrm{in}}$ is the value of $\boldsymbol{\alpha}$ at the initiation of a new loading process as explained in DM04; and μ_0, u are model constants. Default values of $w = 2$ and $\varepsilon = 0{\cdot}01$ are found to be very effective. The exponential term in equation (11) adds stiffness to the deviatoric response by increasing the value of h in analogy to the distance b^{M} of $\boldsymbol{\alpha}$ from its image $\boldsymbol{\alpha}_{\theta}^{\mathrm{M}}$ on the MS, projected on $\boldsymbol{n}$, a standard BS scheme, since the MS is in fact an auxiliary BS for stiffness control. The analytical expression

Table 3. SANISAND-MSf calibrated model constants for two types of sands

Model constant	Symbol	Ottawa-F65	Karlsruhe
Elasticity	G_0	125	100
	ν	0·05	0·05
CSL	M	1·26	1·28
	c	0·735	0·75
	$e_{\mathrm{c}}^{\mathrm{ref}}$	0·78	1·038
	λ_{c}	0·0287	0·056
	ξ	0·7	0·28
Yield surface dilatancy	m	0·01	0·01
	n^{d}	2·50	1·20
	A_0'	0·626	0·56
	n_g	0·9	0·95
Kinematic hardening	n^{b}	0·60	1·0
	h_0'	4·00	7·60
	c_h	0·968	1·015
Fabric dilatancy	$z_{\max}$	15·0	15·0
	c_z	2000	1000
Memory surface	μ_0	4·08	7·80
	u	0·96	0·87
Semifluidised state	c_ℓ	35	25
	x	3·5	3·3
	c_{r}	0*	0*

*Calibration requires detailed data for multiple liquefaction stages.

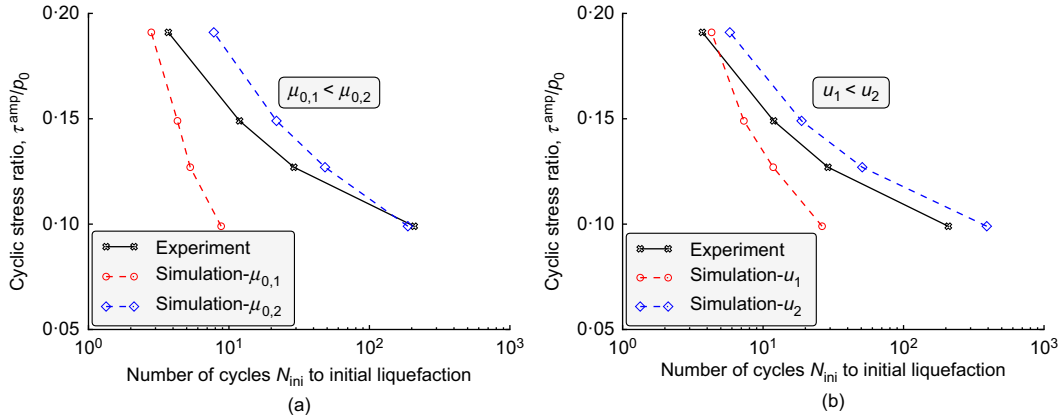

Fig. 6. Effects of SANISAND-MSf model constants μ_0, u on the simulated liquefaction strength curve with initial liquefaction referring to $r_u = 0{\cdot}95$ based on undrained cyclic torsional tests under constant CSR: (a) role of μ_0; (b) role of u

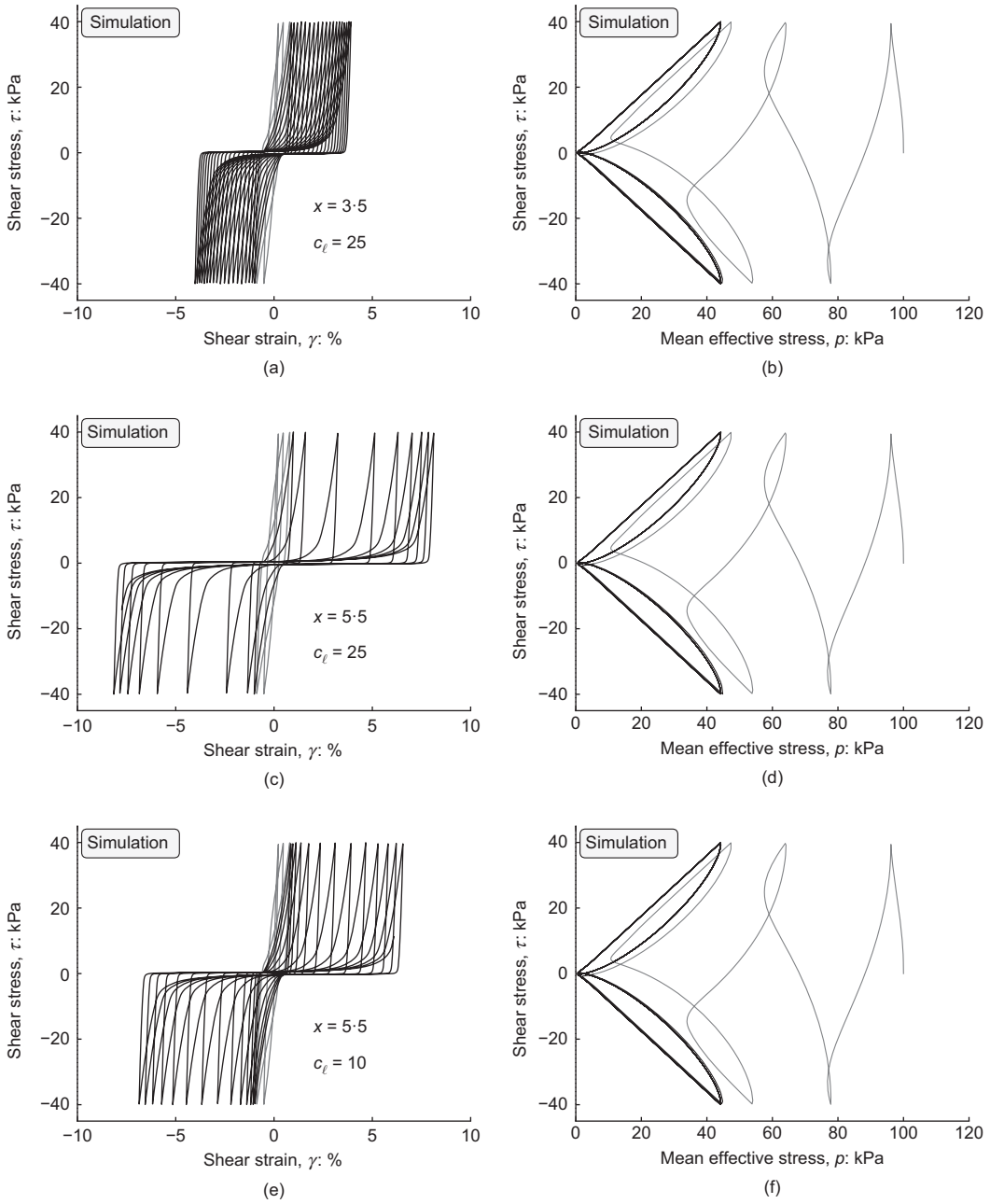

Fig. 7. Effects of SANISAND-MSf model constants in semifluidised state on simulated stress–strain response and effective stress path: (a), (b) $x = 3{\cdot}5$, $c_\ell = 25$; (c), (d) $x = 5{\cdot}5$, $c_\ell = 25$; (e), (f) $x = 5{\cdot}5$, $c_\ell = 10$. Grey and black lines represent pre- and post-liquefaction, respectively

of this exponential term follows an initial suggestion by Liu *et al.* (2019) where the factor $(p/p_{atm})^{0.5}$ of this suggestion, that may adversely affect the simulation of liquefaction resistance with increasing initial p, is substituted by $(||\boldsymbol{\alpha}_{in}||^u + \varepsilon)^{-1}$ that accounts for cyclic shear stress amplitude effects.

SEMIFLUIDISED STATE

Based on the laboratory observations of undrained cyclic shear tests on sand, the concept of 'semifluidised state' is introduced in the paper by Barrero *et al.* (2020), which refers to the state of granular material when the mean effective stress is very small, namely when $p < p_{th}$ with the threshold mean effective stress p_{th} being a model constant. An internal state variable named the 'strain liquefaction factor' (SLF) and symbolised by ℓ is introduced, whose purpose is to induce stiffness degradation within the semifluidised state. The ℓ evolves only when $p < p_{th}$ according to the rate equation

$$\dot{\ell} = \langle L \rangle [c_\ell \langle 1 - p_r \rangle (1 - \ell)^{n_\ell}] - c_r \ell |\dot{\varepsilon}_v| \tag{12}$$

where c_ℓ is a model constant controlling the evolution rate of ℓ; n_ℓ is a model constant with the default value 8·0; the pressure ratio $p_r = p/p_{th}$ compared to 1 determines if the stress state falls into the semifluidised state; and p_{th} is given the default value of 10 kPa, but it can be re-adjusted if necessary for various sands. In regard to such re-adjusted values of p_{th}, a more thorough investigation should be undertaken in the future, possibly using the tool of the discrete-element method. A big advantage of the present scheme is that the analytical dependence of the response on p_{th} is not very sensitive to a more exact and different value of

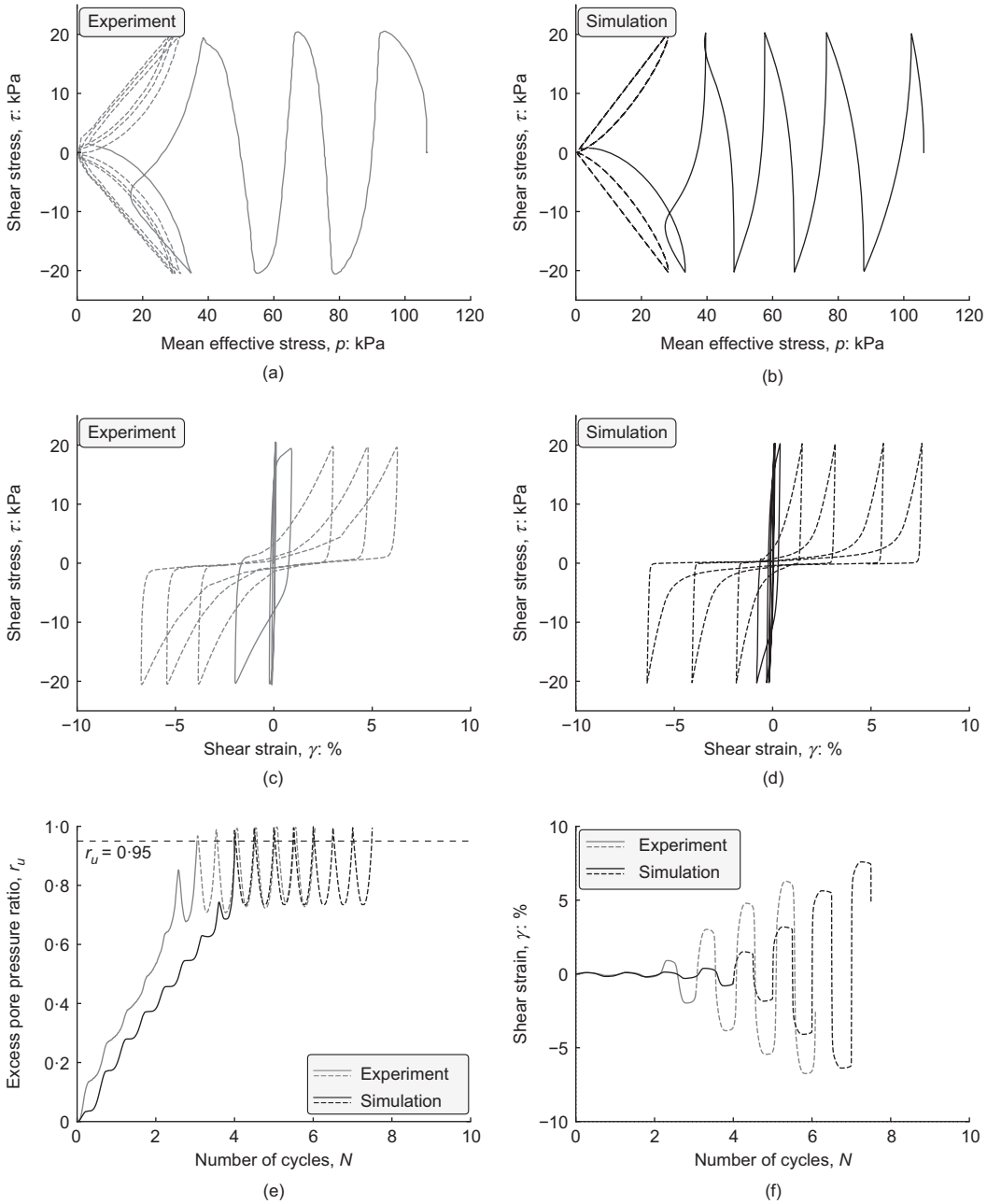

Fig. 8. Simulations compared with experiments in undrained cyclic torsional test with CSR = 0·19 on isotropically consolidated sample of Ottawa-F65 sand with $D_r = 50\%$: (a), (c) experimental data from Ueda *et al.* (2018); (b), (d) simulations using SANISAND-MSf; (e), (f) comparisons between experiments and simulations in terms of pore pressure generation and shear strain development. Experiment and simulation are shown in grey and black lines, respectively. Pre-liquefaction and post-liquefaction are shown in solid and dashed lines, respectively

p_{th}. Because of $\langle 1 - p_r \rangle$ the ℓ evolves from minimum value 0 to maximum value 1 only when $p_r < 1$ within the semi-fluidised state. The last term of equation (12) is zero for undrained loading where $\dot{\varepsilon}_v = 0$, and leads ℓ towards zero during drained loading inside or outside the semifluidised state. This last term is a very important constitutive element because it allows readjustment of ℓ to its initial zero value, and eliminates the shortcoming of various models mentioned in the introduction associated with the use of ever-increasing cumulative quantities such as plastic shear strain for stiffness degradation. The effect of this last term is not addressed in this work because no draining after undrained loading is considered. Yet, one can refer to Barrero *et al.* (2020) for a detailed qualitative investigation of the role of the back-to-zero last term of equation (12) in the response after reaching liquefaction, followed by subsequent drainage and new cyclic loading until re-liquefaction, where the significant effect of the value of model constant c_r is illustrated. Comparison with data is a future necessary endeavour.

The role of the SLF is to decrease by the same factor stiffness and dilatancy, by decreasing the values of h_0 and A_0 listed in Table 1, according to the following two equations:

$$h_0 = h_0' \left[(1 - \langle 1 - p_r \rangle)^{x\ell} + f_\ell \right] \tag{13}$$

$$A_0 = A_0' \left[(1 - \langle 1 - p_r \rangle)^{x\ell} + f_\ell \right] \tag{14}$$

where x and f_ℓ are model constants, the latter with the default value 0·01. The primed quantities h_0' and A_0' are in fact the quantities h_0 and A_0 of the DM04 model, listed in Table 1. The new h_0 of equation (13) will transfer by way of b_0 as listed

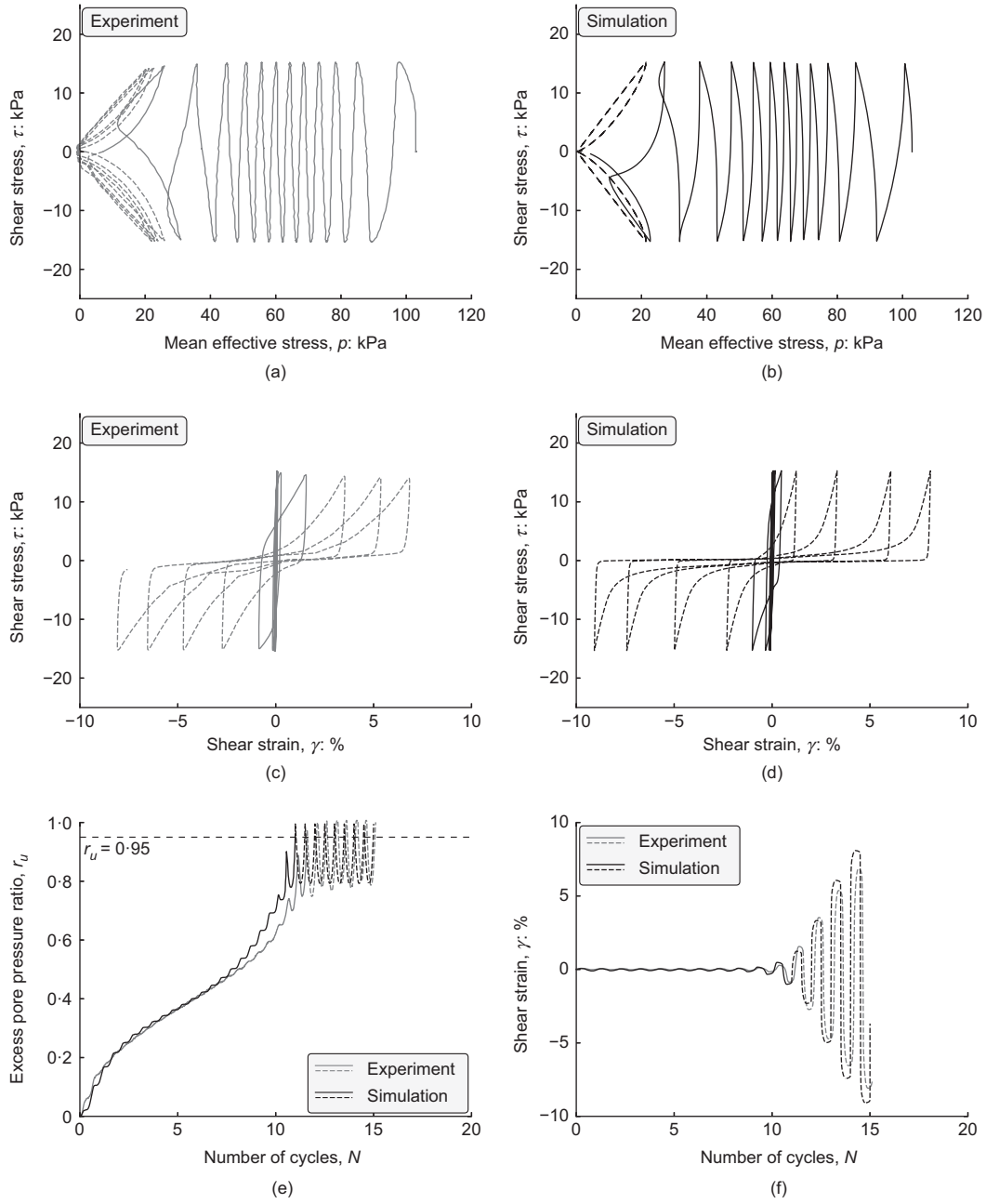

Fig. 9. Simulations compared with experiments in undrained cyclic torsional test with CSR = 0·15 on isotropically consolidated sample of Ottawa-F65 sand with $D_r = 50\%$: (a), (c) experimental data from Ueda *et al.* (2018); (b), (d) simulations using SANISAND-MSf; (e), (f) comparisons between experiments and simulations in terms of pore pressure generation and shear strain development. Experiment and simulation are shown in grey and black lines, respectively. Pre-liquefaction and post-liquefaction are shown in solid and dashed lines, respectively

in Table 1, the effect of ℓ on the value of h in equation (11). Thus, the resulting value of h will be simultaneously affected by the roles of MS and SLF. Observe that outside the semifluidised state one has $p_r = p/p_{th} > 1$, hence, equations (13) and (14) become $h_0 = h_0'(1 + f_\ell)$ and $A_0 = A_0'(1 + f_\ell)$, respectively, rendering h_0 and A_0 almost equal to their original primed values, given the very small default value of $f_\ell = 0{\cdot}01$. Finally, it follows from equations (13) and (14) and the equations of Table 1, that $h_0'/A_0' = h_0/A_0 = K_p/D$, and since the plastic volumetric strain rate is proportional to D/K_p, one has that within the semifluidised state this rate is unaltered by the modifications of h_0' and A_0' to h_0 and A_0, in equations (13) and (14), respectively. This achieves exactly what was intended, based on experimental data, the simulation of which required a strong softening related only to the deviatoric plastic strain rate. Note that the SLF rate equation in the paper by Barrero *et al.* (2020), corresponding to equation (12) in the present work, had an additional term $(p/p_{inr})^a$ to allow for an overall fitting of the liquefaction strength curve based on reaching different cyclic shear strain amplitudes, often inaccurately balanced between pre- and post-liquefaction stages; this is no longer needed given the role of the MS in pre-liquefaction model performance.

Table 2 presents a summary of the transition from the modified DM04 model equations, to those of the new SANISAND-MSf model, in conjunction with the newly introduced constants, including those with default values.

CALIBRATION

The new SANISAND-MSf model requires the calibration of 21 model constants, divided into three groups. The first

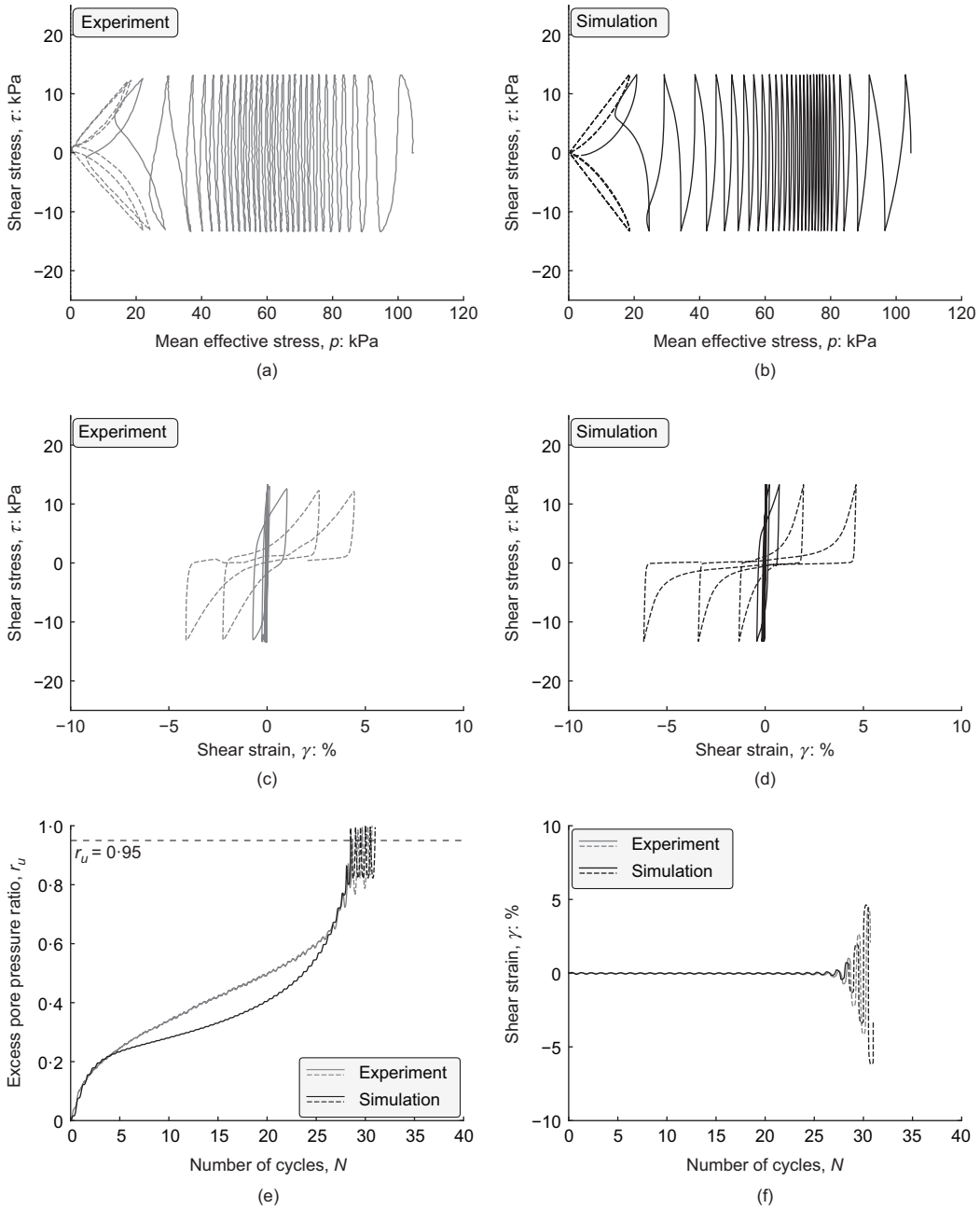

Fig. 10. Simulations compared with experiments in undrained cyclic torsional test with CSR = 0·13 on isotropically consolidated sample of Ottawa-F65 sand with $D_r = 50\%$: (a), (c) experimental data from Ueda *et al.* (2018); (b), (d) simulations using SANISAND-MSf; (e), (f) comparisons between experiments and simulations in terms of pore pressure generation and shear strain development. Experiment and simulation are shown in grey and black lines, respectively. Pre-liquefaction and post-liquefaction are shown in solid and dashed lines, respectively

group includes 16 constants inherited from DM04 and its modification as listed in Table 1; details of their calibration can be found in the paper by Taiebat *et al*. (2010).

The second group is related to the effect of MS on stiffness by means of h, equation (11), and consists of two constants μ_0 and u. Effects of μ_0 and u on the simulated liquefaction strength curve with initial liquefaction referring to $r_u = 0{\cdot}95$ are illustrated in Figs 6(a) and 6(b). It can be concluded that μ_0 mainly affects the position of the liquefaction strength curve, while u affects both the position and the slope.

The last group of model constants, linked to the semi-fluidised state, is used to capture the post-liquefaction shear strain development, without any effect on pre-liquefaction. It consists of c_ℓ and c_r, entering equation (12) and x entering equations (13) and (14). As mentioned after equation (12), the effect of c_r is not addressed in this work, but a parametric study is carried out to illustrate the effect of c_ℓ and x on the post-liquefaction shear strain development. With reference to the typical data of Toyoura sand at $D_r = 70\%$, the numerical results shown in Fig. 7 are obtained with a shear stress amplitude of 40 kPa for three combinations of c_ℓ and x, keeping the other model constants fixed. Based on the foregoing, the following calibration procedure is suggested: (*a*) keep c_ℓ, and vary x to capture the general trend of shear strain development; (*b*) tune c_ℓ for local revision of this general trend towards a better match for each cycle.

MODEL PERFORMANCE

Undrained cyclic torsional tests

The experimental data of undrained stress paths, shear strain development and pore pressure generation under undrained cyclic torsional tests on Ottawa-F65 sand from Ueda *et al*. (2018) will be simulated by the SANISAND-MSf

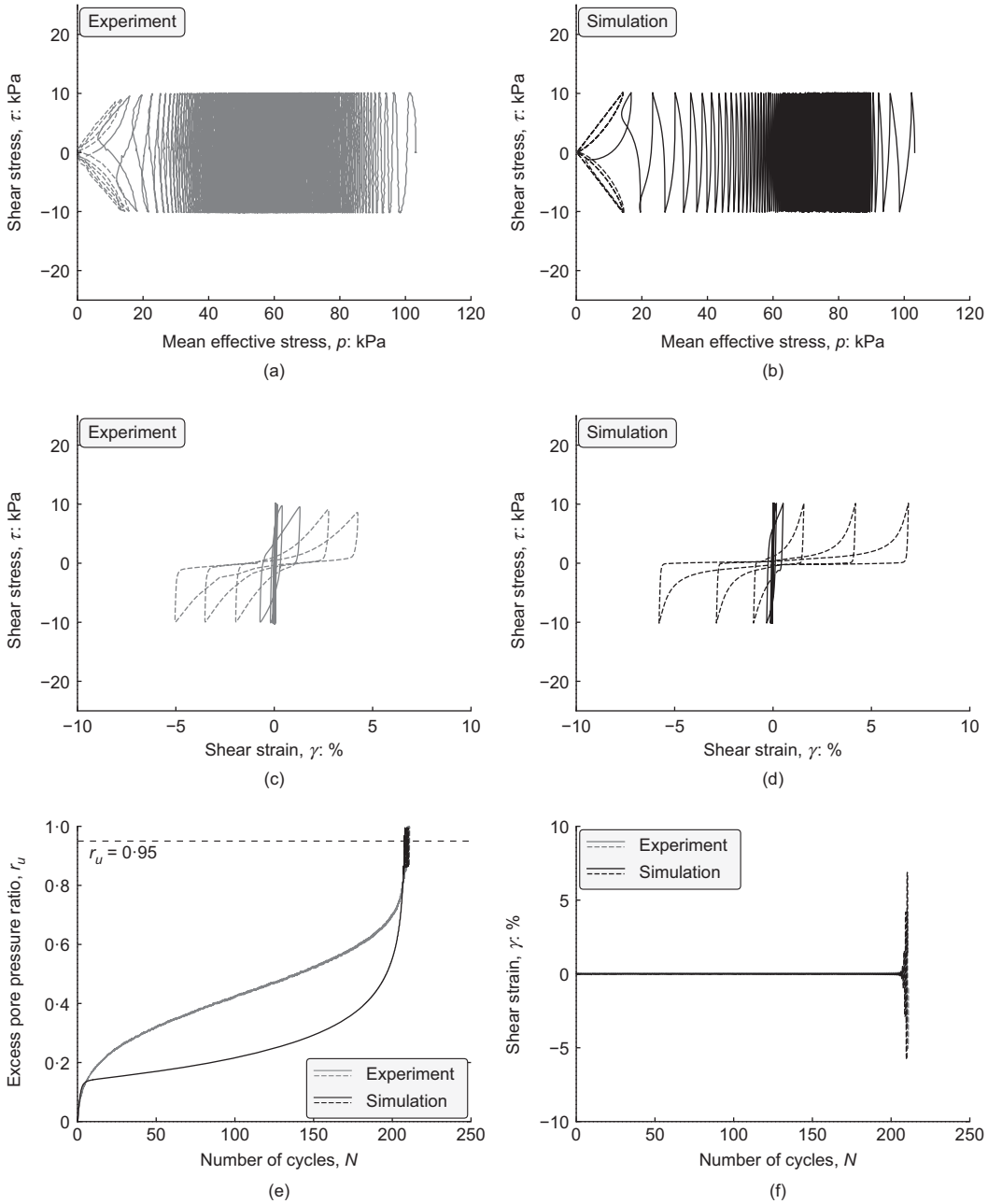

Fig. 11. Simulations compared with experiments in undrained cyclic torsional test with CSR = 0·10 on isotropically consolidated sample of Ottawa-F65 sand with $D_r = 50\%$: (a), (c) experimental data from Ueda *et al.* (2018); (b), (d) simulations using SANISAND-MSf; (e), (f) comparisons between experiments and simulations in terms of pore pressure generation and shear strain development. Experiment and simulation are shown in grey and black lines, respectively. Pre-liquefaction and post-liquefaction are shown in solid and dashed lines, respectively

model. The samples are isotropically consolidated at around 100 kPa, ending up with very similar relative densities of 50%. Four tests are carried out with CSR values of 0·19, 0·15, 0·13 and 0·10. Recall that here CSR $= \tau^{amp}/p_0$. The model constants are provided in Table 3 with most inherited from the DM04 model, as determined in Ramirez *et al.* (2018), while z_{max} and c_z are tuned for better approaching the semifluidised state. The other model constants related to MS and semifluidised state are calibrated by following the aforementioned procedures in the calibration section.

Figures 8–11 present experiments and simulations for the aforementioned four CSRs. The loading process is divided into two stages, before and after the excess pore pressure ratio $r_u = 0{\cdot}95$, for the first time so that the comparisons can be made separately for pre- and post-liquefaction stages – shown in solid and dashed lines, respectively. Such comparisons are in general quite satisfactory, as clearly shown in the figures, and the following few points can be emphasised. As the CSR becomes progressively smaller, the model can capture the increasing number of cycles during the pre-liquefaction stage, shown by the solid lines of the parts (b) as compared with the corresponding experimental curves of the parts (a) of Figs 8–11. In particular Fig. 11(b) compared with Fig. 11(a) presents successful simulations for the very low CSR = 0·10 that are beyond the capabilities of most existing constitutive models, including DM04, but for SANISAND-MSf the ingredient of the MS allows over 200 cycles to be captured in the pre-liquefaction stage, until $r_u = 0{\cdot}95$ is reached. Similarly, owing to the constitutive ingredient of the semifluidised state, the model can capture the increasing

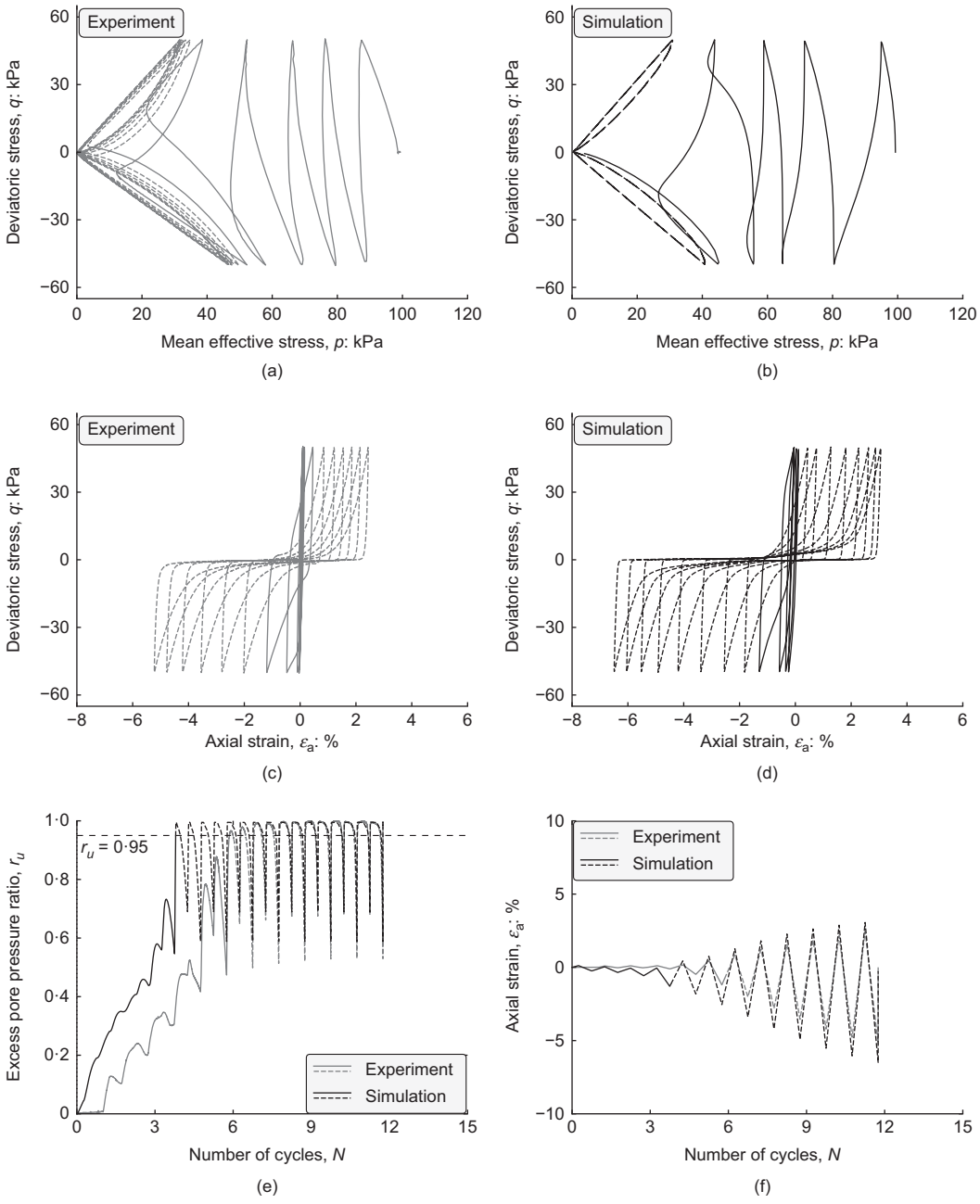

Fig. 12. Simulations compared with experiments in undrained cyclic triaxial test with CSR = 0·25 on isotropically consolidated sample of Karlsruhe find sand with $D_r = 79\%$: (a), (c) experimental data from Wichtmann & Triantafyllidis (2016); (b), (d) simulations using SANISAND-MSf; (e), (f) comparisons between experiments and simulations in terms of pore pressure generation and axial strain development. Experiment and simulation are shown in grey and black lines, respectively. Pre-liquefaction and post-liquefaction are shown in solid and dashed lines, respectively

shear strain amplitude in the post-liquefaction stage, shown by the dashed lines of parts (d) in comparison with the experiments of parts (c) in Figs 8–11. Characteristically Fig. 9(d) shows a slowdown of the strain amplitude increase, exactly as exhibited by the data in Fig. 9(c), and this is the result of the SLF ℓ approaching its saturation value of 1. Parts (e) and (f) of Figs 8–11 illustrate the successful simulations of the previous parts from the perspective of pore water pressure and shear strain amplitude variations plotted against the number of cycles for the four different CSRs.

Undrained cyclic triaxial tests

Data of undrained cyclic triaxial loading on Karlsruhe fine sand from Wichtmann & Triantafyllidis (2016) will be simulated by the SANISAND-MSf model. The sand samples are isotropically consolidated around 100 kPa, ending up with similar relative densities around $D_r \approx 78\%$. Three experimental tests are carried out with different CSRs of 0·25, 0·20 and 0·15. Here CSR $= q^{amp}/(2p_0)$, that is, the ratio of the deviatoric stress amplitude to twice the initial mean effective stress. The calibrated model constants are provided in Table 3 with most related to the DM04 model and adopted from Liu *et al.* (2018), while the others are calibrated as mentioned in the calibration section.

Figures 12–14 present data and simulations for the aforementioned CSRs. The asymmetries of the undrained stress path butterfly shapes in parts (b) and stress–strain loops in parts (d) of these figures are in agreement with the corresponding experimental data of parts (a) and (c), respectively, and result from setting the model constant $c =$ 0·712, while size-wise the simulated strain is close to the data

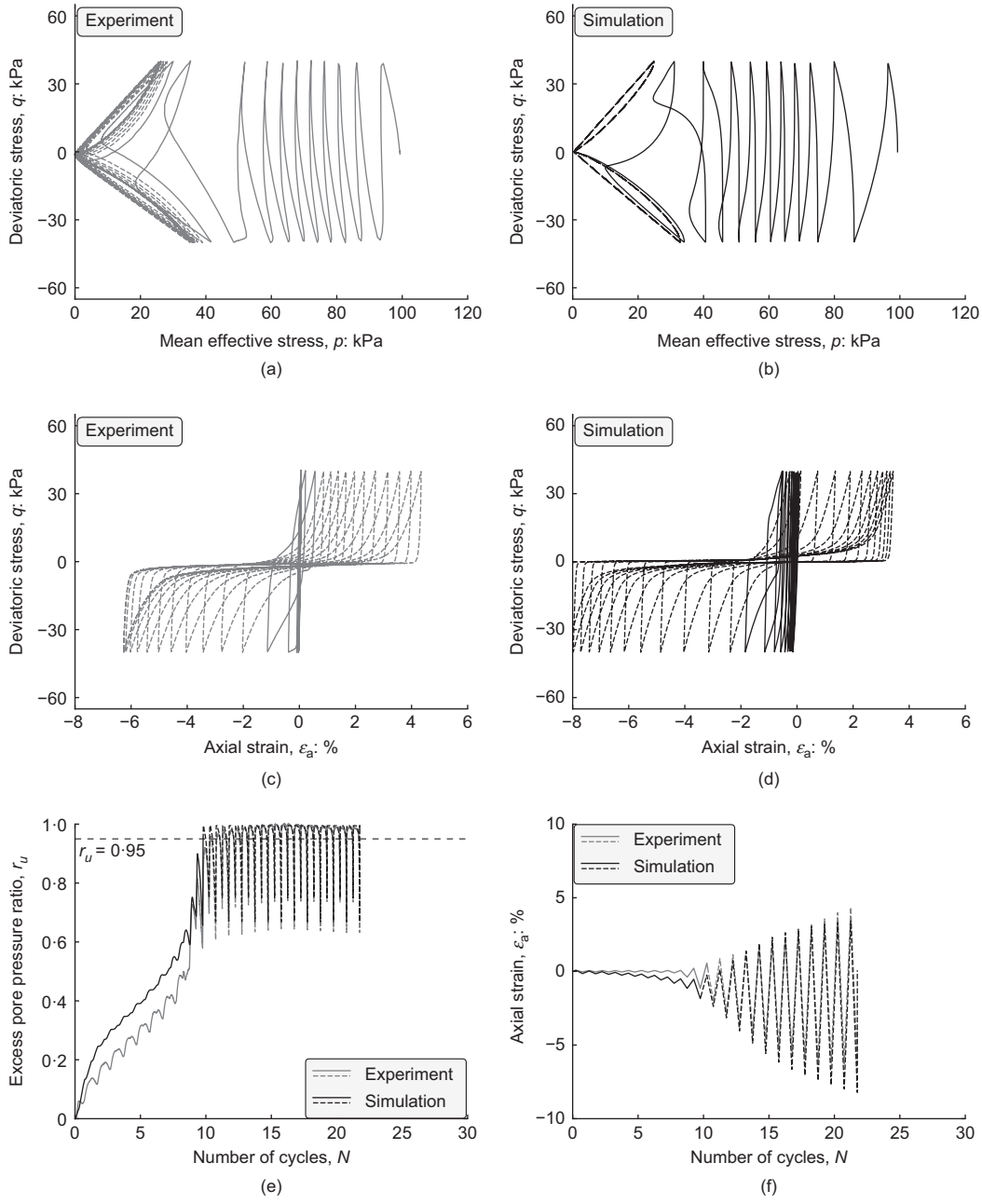

Fig. 13. Simulations compared with experiments in undrained cyclic triaxial test with CSR = 0·20 on isotropically consolidated sample of Karlsruhe find sand with $D_r = 78\%$: (a), (c) experimental data from Wichtmann & Triantafyllidis (2016); (b), (d) simulations using SANISAND-MSf; (e), (f) comparisons between experiments and simulations in terms of pore pressure generation and axial strain development. Experiment and simulation are shown in grey and black lines, respectively. Pre-liquefaction and post-liquefaction are shown in solid and dashed lines, respectively

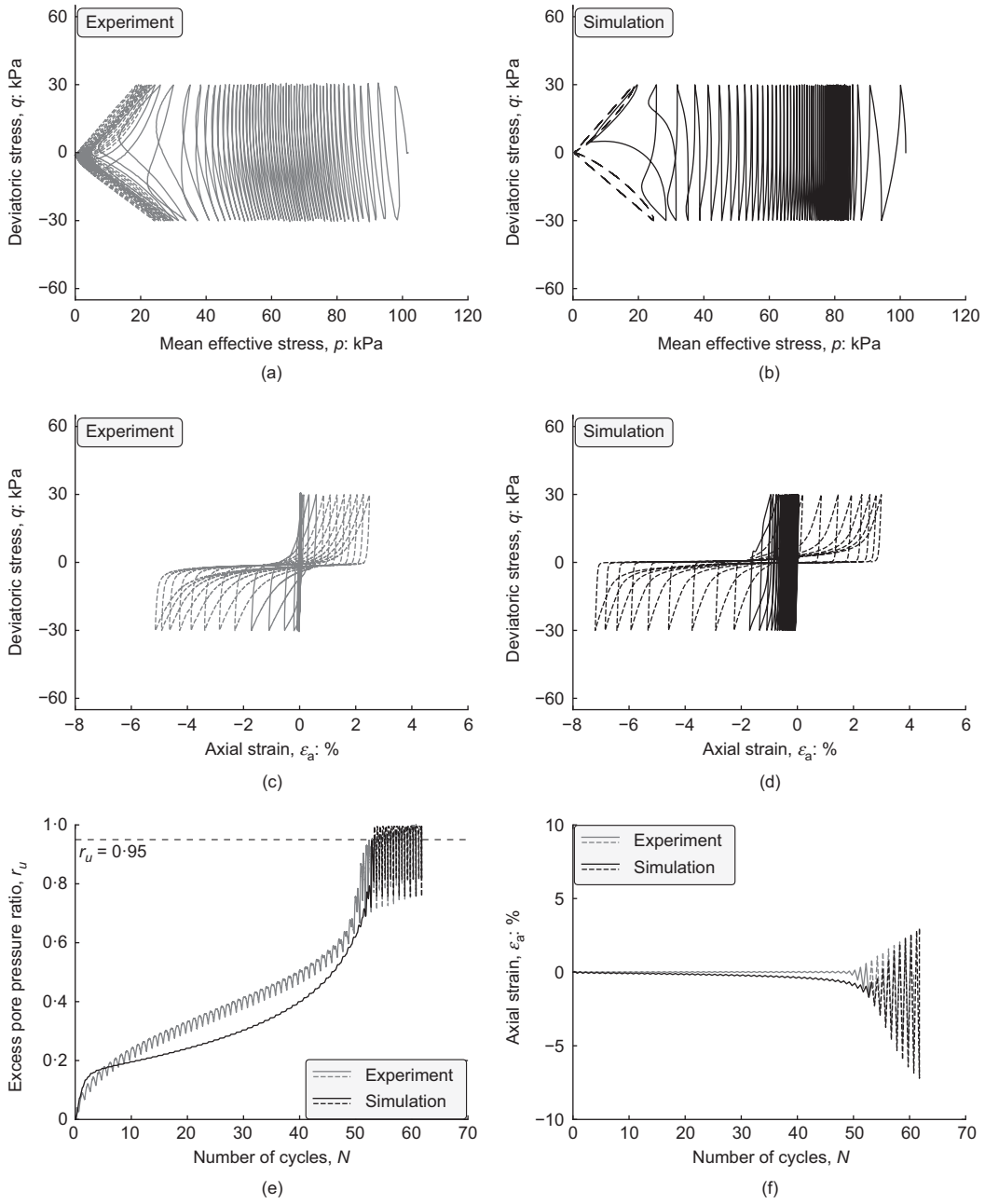

Fig. 14. Simulations compared with experiments in undrained cyclic triaxial test with CSR = 0·15 on isotropically consolidated sample of Karlsruhe find sand with $D_r = 78\%$: (a), (c) experimental data from Wichtmann & Triantafyllidis (2016); (b), (d) simulations using SANISAND-MSf; (e), (f) comparisons between experiments and simulations in terms of pore pressure generation and axial strain development. Experiment and simulation are shown in grey and black lines, respectively. Pre-liquefaction and post-liquefaction are shown in solid and dashed lines, respectively

thanks to the incorporation of the semifluidised state. For the same reason of $c = 0{\cdot}712$, one has the shifting of the stress–strain loops towards extension observed experimentally in parts (c) and successfully simulated in parts (d) of Figs 12–14. Such shifting is controlled by the introduction of $g(\theta, c)^{n_g}$ in the modification of the DM04 shown in Table 1, and had it not been introduced, the shifting would have been unrealistically larger. Observe that shifting of the stress–strain loops in Figs 13(d) and 14(d) towards extension is slightly larger than the data, and this can be attributed to the shifting occurring in the pre-liquefaction stage, shown by the solid line loops. In conclusion, the successful simulation of undrained stress paths, and the pore pressure generation and shear strain development in both pre- and post-liquefaction stages, further confirm that the SANISAND-MSf model can address the main ingredients of granular material under undrained cyclic triaxial shearing.

Liquefaction strength curve

The liquefaction strength curve – that is, the plot of CSR against the number of cycles to initial liquefaction – is a different perspective and a practically important measure of the success of a simulation. The foregoing data and simulations will be used to plot the corresponding strength curves, adopting four criteria for initial liquefaction, namely one r_u based and three shear strain based.

Figure 15 presents the liquefaction strength curves for the four undrained cyclic torsional tests on Ottawa F65 sand with $D_r = 50\%$. The criteria for the initial liquefaction are

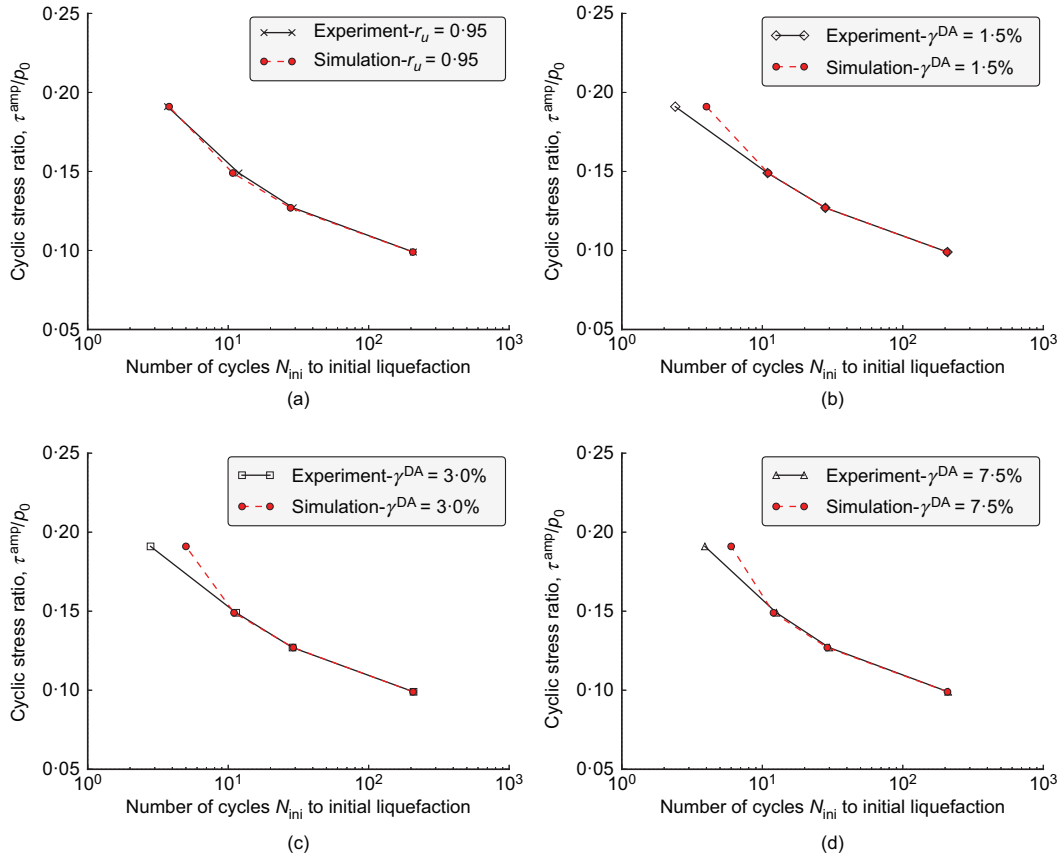

Fig. 15. Liquefaction strength curves on Ottawa-F65 sand with $D_r = 50\%$: (a) $r_u = 0{\cdot}95$; (b) $\gamma^{DA} = 1{\cdot}5\%$; (c) $\gamma^{DA} = 3{\cdot}0\%$; (d) $\gamma^{DA} = 7{\cdot}5\%$

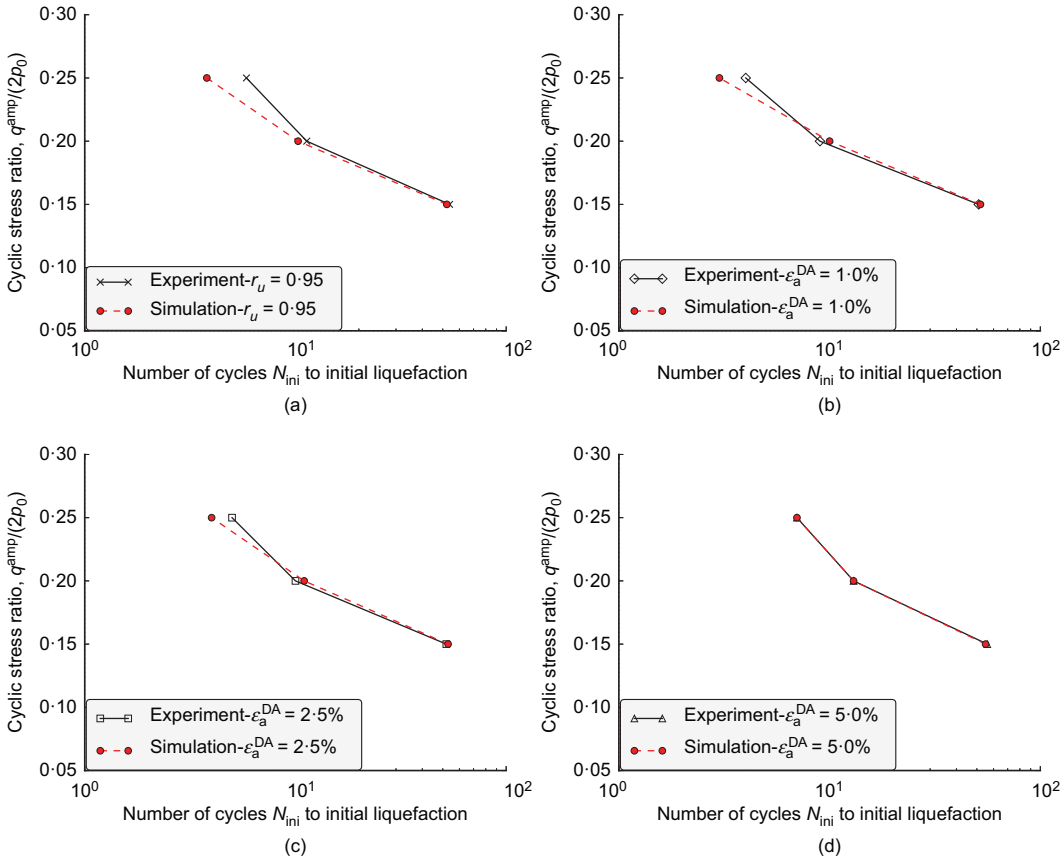

Fig. 16. Liquefaction strength curves on Karlsruhe fine sand with $D_r \approx 78\%$: (a) $r_u = 0{\cdot}95$; (b) $\varepsilon_a^{DA} = 1{\cdot}0\%$; (c) $\varepsilon_a^{DA} = 2{\cdot}5\%$; (d) $\varepsilon_a^{DA} = 5{\cdot}0\%$

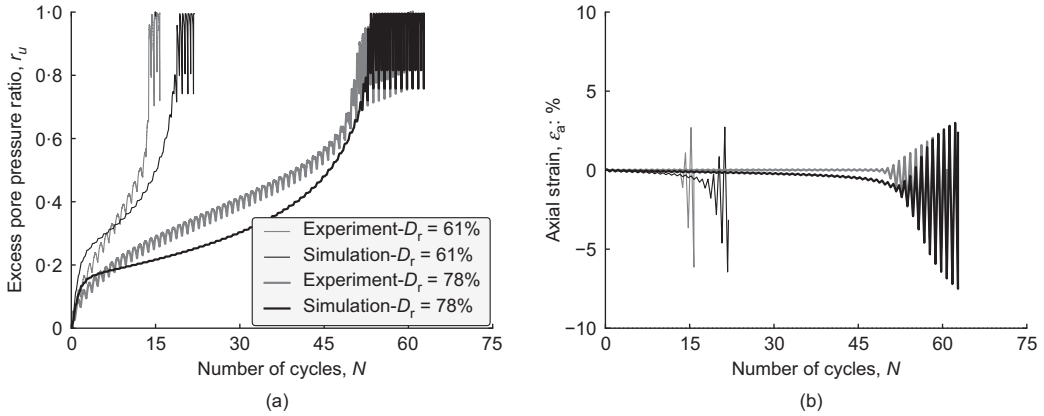

Fig. 17. SANISAND-MSf model performance in simulating effect of initial relative density D_r on isotropically consolidated samples of Karlsruhe fine sand with $p_0 = 100$ kPa and CSR = 0·15: (a) pore pressure generation; (b) axial strain development

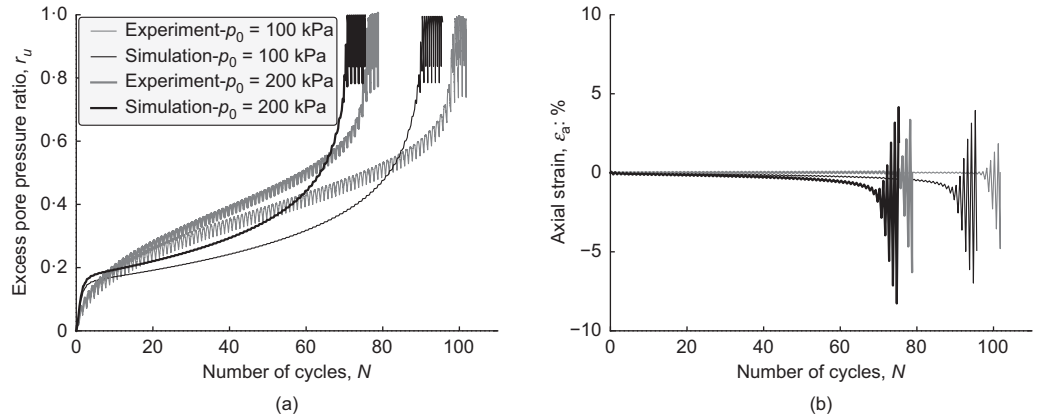

Fig. 18. SANISAND-MSf model performance in simulating effect of initial pressure p_0 on isotropically consolidated samples of Karlsruhe fine sand with $D_r \approx 65\%$ and CSR = 0·125: (a) pore pressure generation; (b) axial strain development

excess pore pressure ratio, $r_u = 0{\cdot}95$, and three double amplitudes of shear strain, namely $\gamma^{DA} = 1{\cdot}5\%$, $\gamma^{DA} = 3{\cdot}0\%$ and $\gamma^{DA} = 7{\cdot}5\%$. The data imply that $r_u = 0{\cdot}95$ happens between $\gamma^{DA} = 3{\cdot}0\%$ and $\gamma^{DA} = 7{\cdot}5\%$, while the model suggests a value of around 1·5%. The model can give very precise simulation of the number of cycles for $r_u = 0{\cdot}95$ for all CSRs, as seen in Fig. 15(a). For the three shear-strain-based criteria the model slightly over-predicts the number of cycles, with small variations between higher and lower CSRs. In general, the performance is very satisfactory.

Figure 16 presents the liquefaction strength curve for the three undrained cyclic triaxial tests on Karlsruhe fine sand with $D_r \approx 78\%$. The four criteria for initial liquefaction are excess pore pressure ratio $r_u = 0{\cdot}95$, and three double amplitudes of axial strain $\varepsilon_a^{DA} = 1{\cdot}0\%$, $\varepsilon_a^{DA} = 2{\cdot}5\%$ and $\varepsilon_a^{DA} = 5{\cdot}0\%$. The data imply that $r_u = 0{\cdot}95$ happens between $\varepsilon_a^{DA} = 2{\cdot}5\%$ and $\varepsilon_a^{DA} = 5{\cdot}0\%$, while the model suggests a range between $\varepsilon_a^{DA} = 1{\cdot}0\%$ and $\varepsilon_a^{DA} = 2{\cdot}5\%$. For all four criteria the data and simulations are in good agreement on the average for all CSRs, with some small over-prediction of the number of cycles for the strain-based criteria, except from the test with the lowest CSR, which exhibits the excellent performance shown in Figs 16(b)–16(d). The experiments from Figs 15 and 16 indicate that large deformation occurs along with excess pore pressure ratio approaching 0·95, irrespective of which criterion is adopted for initial liquefaction. This message is also conveyed by the present model.

Effect of initial conditions

While the foregoing has addressed simulations for various values of CSR at the same initial relative density D_r and mean stress p_0, the following addresses simulations for different values of D_r and p_0 under the same constant CSR. Various laboratory experiments (Vaid *et al.*, 2001; Hyodo *et al.*, 2002; Kiyota *et al.*, 2008; Yang & Sze, 2011; Wichtmann & Triantafyllidis, 2016) indicate that cyclic liquefaction resistance increases with increasing relative density or decreasing initial mean stress.

Figure 17 compares simulation and experimental plots of pore pressure generation and axial strain development against number of cycles, for two undrained cyclic triaxial tests on isotropically consolidated samples of Karlsruhe fine sand with the same $p_0 = 100$ kPa but different relative densities subjected to a CSR of 0·15. Similarly, Fig. 18 compares same plots of experiments and simulations of two undrained cyclic triaxial tests on isotropically consolidated samples of Karlsruhe fine sand with similar $D_r \approx 65\%$ but different initial mean stresses under a CSR of 0·125. The reasonable agreement between simulations and experimental data in Figs 17 and 18 shows that SANISAND-SMf is capable of capturing the effects of different initial densities and mean stresses.

CONCLUSION

The new SANISAND-MSf constitutive model for sands is formulated by introducing minor and major modifications

into the DM04 model platform by Dafalias & Manzari (2004). The minor modification consists of two parts: one that improves the accuracy of the non-associative flow rule in non-proportional loading, and a second that improves the cyclic shear stress–strain loops shifting under cyclic triaxial loading by introducing a simple Lode angle dependence. The major modification also has two parts, incorporating two new constitutive ingredients. The first is a back-stress-ratio-based MS, which is a drastic modification of the original idea proposed by Corti *et al*. (2016) and adjusted by Liu *et al*. (2019) to align with the DM04 model. The role of the MS is to increase the stiffness for back-stress ratios within it, in order to better simulate the stress paths and stress–strain loops for undrained cyclic shear tests in the pre-liquefaction stage. Compared to the foregoing references, the present MS ingredient addresses several important issues, among them a size of zero initial value, greater simplicity and generality of its evolution and the avoidance of singularity occurring by possible zeroing of a denominator in the formulation. The second constitutive ingredient is the concept of a semifluidised state for very low effective stresses (Barrero *et al*., 2020), within which strong stiffness and dilatancy degradation is described by means of an evolving state variable termed the SLF, which can simulate large shear strain development in the post-liquefaction stage without affecting the response in the pre-liquefaction stage. The SANISAND-MSf model is validated against two experimental databases – namely, four undrained cyclic torsional tests and three undrained cyclic triaxial tests. The simulations of the undrained stress path, stress–strain loops, excess pore pressure generation and shear strain development plotted against the number of cycles are successfully compared with the experimental data. Furthermore, and unlike other models, such simulation is successful separately for the pre- and post-liquefaction stages. The corresponding strength curves of CSR plotted against number of cycles to initial liquefaction, the latter defined in terms of both r_u-based and shear-strain-based criteria, show very satisfactory comparisons with data, thus removing a simulation shortcoming of the reference base DM04 model. The constitutive ingredients of MS and semifluidised state have generic value and can be incorporated in other models, similar to the DM04 model, such as the zero elastic range model developed and implemented by Dafalias & Taiebat (2016) and Petalas & Dafalias (2019), with appropriate adjustments.

It is also expected that the model will perform satisfactorily under drained cyclic conditions, as shown for similar formulations by Corti *et al*. (2016) and Liu *et al*. (2019), and this will be addressed in future works. Simulations under undrained cyclic loading, however, remain the most useful and difficult to achieve, and it is believed that the present work has contributed positively in this endeavour. With such satisfactory performance in simulating unidirectional cyclic shear tests, the next step is to conduct a systematic evaluation of SANISAND-MSf with respect to multidirectional cyclic shear tests (Yang *et al*., 2019), where effects of initial static bias and different cyclic shear paths are considered.

The present model is void of two common theoretical shortcomings with practical implications, encountered in other constitutive models with similar simulative capabilities. First, it does not use quantities that depend on cumulative shear strain to describe stiffness degradation, which remain in the model affecting unduly the subsequent loading simulations. Instead, the SLF is introduced within the concept of a semifluidised state, which promptly fades away upon drainage following the cyclic loading. Second, it does not include quantities related to the initiation of a cyclic loading, such as the initial value p_0 of p or the CSR that includes p_0, into the constitutive relations; models which do fall into the trap that any intermediate state can be virtually considered as an initial loading state, by means of a stop-and-start-again loading event, thus, adversely modify the subsequent response for what is essentially the same loading process. Instead, only updatable values of internal variables at the initiation of any new plastic loading process are used, such as α_{in}, and it was shown that the model is capable of capturing the effect of different initial conditions on density and mean pressure.

Thermodynamic compatibility in the sense of positive dissipation (positive entropy production) is a desired feature not always addressed in inelastic constitutive modelling works, as in the present one. One way this can be achieved requires making hypotheses about the structure of free energy dependence on internal variables that in conjunction with the rate evolution equations of these variables are sufficient to satisfy positive dissipation, but one may expect restrictions on the constants of those equations. In the case of kinematic hardening internal variables, a basic feature of the present model family, there is a standard approach that can be found in the paper by Feigenbaum & Dafalias (2008) for metals which, however, will require adjustments to accommodate the dilatancy feature for soils that does not exist in metals. An effort in this direction will be undertaken in the future.

ACKNOWLEDGEMENTS

Support for this study was provided by the Natural Sciences and Engineering Research Council of Canada (NSERC). Y. F. Dafalias acknowledges support by the General Secretariat for Research and Technology of Greece and NTUA under the projects titled SOFIL and SOFAD, respectively, the European Regional Development Fund under grant no. CZ.02·1·01/0·0/0·0/15-003/0000493, CeNDYNMAT, Czech Republic and the US Army Research Laboratory and US Army Research Office under grant no. W911NF-19-1-0040.

NOTATION

A_0	dilatancy model variable in equation (14)
A_0'	dilatancy model constant
B	model variable in Table 1
b_0	plastic modulus model variable in Table 1
b^{M}	projection distance between $\boldsymbol{\alpha}_\theta^{\text{M}}$ and $\boldsymbol{\alpha}$ along $\boldsymbol{n}$
b_{ref}	bounding surface length along $\boldsymbol{n}$
C	model variable in Table 1
c	Lode angle interpolation constant
c_h	plastic modulus model constant
c_ℓ	semifluidised state model constant
c_{r}	semifluidised state model constant
c_z	fabric dilatancy model constant
D	dilatancy
D_{r}	relative density
e	void ratio
e_{c}	critical void ratio
$e_{\text{c}}^{\text{ref}}$	critical state line model constant
$\boldsymbol{e}^{\text{e}}$	elastic deviatoric strain tensor
$\boldsymbol{e}^{\text{p}}$	plastic deviatoric strain tensor
f	yield surface
f_ℓ	semifluidised state model constant with a default value of 0·01
f^{M}	memory surface
G	hypoelasticity shear modulus
G_0	hypoelasticity model constant
$g(\theta, c)$	Lode-angle-dependent interpolation function
h	hardening coefficient for kinematic hardening
h^*	user-defined constant for determination of h^{M}
h_0	model variable in equation (13)
h_0'	plastic modulus model constant

h^{M} hardening coefficient for memory surface kinematic hardening in equation (7)
$I(x_\alpha)$ interpolation function in equation (1)
$\boldsymbol{I}$ second-order identity tensor
K hypoelasticity bulk modulus
K_{p} plastic modulus
ℓ strain liquefaction factor in equation (12)
L plastic multiplier
M critical state stress ratio in p–q space
m yield surface size model constant
m^{M} memory surface size model variable
N number of loading cycles
N_{ini} number of loading cycles to initial liquefaction
$\boldsymbol{n}$ unit norm tensor normal to yield surface
n^{b} bounding surface model constant
n^{d} dilatancy model constant
n_g model constant in Table 1
n_ℓ semifluidised state model constant with a default value of 8·0
$\boldsymbol{n}_\alpha$ unit norm tensor along α
p mean effective stress
p_0 initial mean effective stress
p_{at} atmospheric pressure
p_{r} threshold pressure ratio
p_{th} threshold pressure with a default value of 10 kPa
q deviatoric stress
$\boldsymbol{R}'$ deviatoric flow rule tensor of DM04 model
$\boldsymbol{R}^*$ deviatoric flow rule tensor of current model in equation (1)
$\boldsymbol{r}$ deviatoric stress ratio tensor
r_u excess pore water pressure ratio
$\boldsymbol{s}$ deviatoric stress tensor
u memory surface model constant in equation (11)
w memory surface model constant with a default value of 2·0 in equation (11)
x semifluidised state model constant
x_α relative distance between $\alpha^{\mathrm{b}}_{\theta_\alpha}$ and α
$\boldsymbol{z}$ fabric dilatancy tensor
$z_{\max}$ fabric dilatancy model constant
$\boldsymbol{\alpha}$ yield surface centre tensor
$\boldsymbol{\alpha}_{\mathrm{in}}$ value of $\boldsymbol{\alpha}$ at initiation of new loading
$\boldsymbol{\alpha}^{\mathrm{M}}$ memory surface centre tensor
$\boldsymbol{\alpha}^{\mathrm{b}}_\theta$ projection of $\boldsymbol{\alpha}$ on bounding surface along $\boldsymbol{n}$
$\boldsymbol{\alpha}^{\mathrm{bM}}_\theta$ bounding target of $\boldsymbol{\alpha}^{\mathrm{M}}$
$\alpha^{\mathrm{b}}_{\theta_\alpha}$ length of $\boldsymbol{\alpha}^{\mathrm{b}}_{\theta_\alpha}$
$\boldsymbol{\alpha}^{\mathrm{b}}_{\theta_\alpha}$ projection of $\boldsymbol{\alpha}$ on bounding surface along $\boldsymbol{n}_\alpha$
$\boldsymbol{\alpha}^{\mathrm{b}}_{\theta+\pi}$ projection of $\boldsymbol{\alpha}$ on bounding surface along $-\boldsymbol{n}$
$\boldsymbol{\alpha}^{\mathrm{d}}_\theta$ projection of $\boldsymbol{\alpha}$ on dilatancy surface along $\boldsymbol{n}$
$\boldsymbol{\alpha}^{\mathrm{M}}_\theta$ projection of $\boldsymbol{\alpha}$ on memory surface along $\boldsymbol{n}$
γ shear strain
$\boldsymbol{\varepsilon}$ strain tensor
ε_{a} axial strain
ε_{v} volumetric strain
$\varepsilon^{\mathrm{e}}_{\mathrm{v}}$ elastic volumetric strain
$\varepsilon^{\mathrm{p}}_{\mathrm{v}}$ plastic volumetric strain
ς memory surface shrinkage model constant
θ Lode angle along $\boldsymbol{n}$
θ_α Lode angle along $\boldsymbol{n}_\alpha$
λ_{c} critical state line model constant
μ_0 memory surface model constant in equation (11)
ν hypoelasticity Poisson's ratio
ξ critical state line model constant
$\boldsymbol{\sigma}$ stress tensor
τ shear stress
τ^{amp} amplitude of shear stress
ψ state parameter

REFERENCES

Barrero, A. R., Taiebat, M. & Dafalias, Y. F. (2020). Modeling cyclic shearing of sands in semifluidized regime. *Int. J. Numer. Analyt. Methods Geomech.* **44**, No. 3, 371–388.

Been, K. & Jefferies, M. G. (1985). A state parameter for sands. *Géotechnique* **35**, No. 2, 99–112, https://doi.org/10.1680/geot.1985.35.2.99.

Boulanger, R. W. & Ziotopoulou, K. (2013). Formulation of a sand plasticity plane-strain model for earthquake engineering applications. *Soil Dyn. Earthq. Engng* **53**, 254–267.

Castro, G. (1975). Liquefaction and cyclic mobility of saturated sands. *J. Geotech. Engng Div.* **101**, No. GT6, 551–569.

Corti, R., Diambra, A., Wood, D. M., Escribano, D. E. & Nash, D. F. T. (2016). Memory surface hardening model for granular soils under repeated loading conditions. *J. Engng Mech.* **142**, No. 12, 04016102.

Dafalias, Y. F. (1986). Bounding surface plasticity. I: Mathematical foundation and hypoplasticity. *J. Engng Mech.* **112**, No. 9, 966–987.

Dafalias, Y. F. & Manzari, M. T. (2004). Simple plasticity sand model accounting for fabric change effects. *J. Engng Mech.* **130**, No. 6, 622–634.

Dafalias, Y. F. & Taiebat, M. (2016). SANISAND-Z: zero elastic range sand plasticity model. *Géotechnique* **66**, No. 12, 999–1013, https://doi.org/10.1680/jgeot.15.P.271.

di Benedetto, H., Blanc, M., Tiouajni, S. & Ezaoui, A. (2014). Elastoplastic model with loading memory surfaces (LMS) for monotonic and cyclic behaviour of geomaterials. *Int. J. Numer. Analyt. Methods Geomech.* **38**, No. 14, 1477–1502.

Elgamal, A., Yang, Z., Parra, E. & Ragheb, A. (2003). Modeling of cyclic mobility in saturated cohesionless soils. *Int. J. Plast.* **19**, No. 6, 883–905.

Feigenbaum, H. P. & Dafalias, Y. F. (2008). Simple model for directional distortional hardening in metal plasticity within thermodynamics. *J. Engng Mech.* **134**, No. 9, 730–738.

Hyodo, M., Hyde, A. F., Aramaki, N. & Nakata, Y. (2002). Undrained monotonic and cyclic shear behaviour of sand under low and high confining stresses. *Soils Found.* **42**, No. 3, 63–76.

Khosravifar, A., Elgamal, A., Lu, J. & Li, J. (2018). A 3D model for earthquake-induced liquefaction triggering and post-liquefaction response. *Soil Dyn. Earthq. Engng* **110**, 43–52.

Kiyota, T., Sato, T., Koseki, J. & Abadimarand, M. (2008). Behavior of liquefied sands under extremely large strain levels in cyclic torsional shear tests. *Soils Found.* **48**, No. 5, 727–739.

Li, X. S. & Wang, Y. (1998). Linear representation of steady-state line for sand. *J. Geotech. Geoenviron. Engng* **124**, No. 12, 1215–1217.

Liu, H. Y., Zygounas, F., Diambra, A. & Pisano, F. (2018). Enhanced plasticity modelling of high-cyclic ratcheting and pore pressure accumulation in sands. In *Numerical methods in geotechnical engineering IX, volume 1: proceedings of the 9th European conference on numerical methods in geotechnical engineering (NUMGE 2018)* (eds A. S. Cardoso, J. L. Borges, P. A. Costa, A. T. Gomes, J. C. Marques and C. S. Vieira), pp. 87–96. Leiden, the Netherlands: CRC Press/Balkema.

Liu, H. Y., Abell, J. A., Diambra, A. & Pisanó, F. (2019). Modeling the cyclic ratcheting of sands through memory-enhanced bounding surface plasticity. *Géotechnique* **69**, No. 9, 783–800, https://doi.org/10.1680/jgeot.17.P.307.

Maleki, M., Cambou, B. & Dubujet, P. (2009). Development in modeling cyclic loading of sands based on kinematic hardening. *Int. J. Numer. Analyt. Methods Geomech.* **33**, No. 14, 1641–1658.

Manzari, M. T. & Dafalias, Y. F. (1997). A critical state two-surface plasticity model for sands. *Géotechnique* **47**, No. 2, 255–272, https://doi.org/10.1680/geot.1997.47.2.255.

Papadimitriou, A. G. & Bouckovalas, G. D. (2002). Plasticity model for sand under small and large cyclic strains: a multiaxial formulation. *Soil Dyn. Earthq. Engng* **22**, No. 3, 191–204.

Papadimitriou, A. G., Bouckovalas, G. D. & Dafalias, Y. F. (2001). Plasticity model for sand under small and large cyclic strains. *J. Geotech. Geoenviron. Engng* **127**, No. 11, 973–983.

Petalas, A. L. & Dafalias, Y. F. (2019). Implicit integration of incrementally non-linear, zero-elastic range, bounding surface plasticity. *Comput. Geotech.* **12**, 386–402.

Ramirez, J., Barrero, A. R., Chen, L., Dashti, S., Ghofrani, A., Taiebat, M. & Arduino, P. (2018). Site response in a layered liquefiable deposit: evaluation of different numerical tools and methodologies with centrifuge experimental results. *J. Geotech. Geoenviron. Engng* **144**, No. 10, 04018073.

Stallebrass, S. E. & Taylor, R. N. (1997). The development and evaluation of a constitutive model for the prediction of ground

movements in overconsolidated clay. *Géotechnique* **47**, No. 2, 235–253, https://doi.org/10.1680/geot.1997.47.2.235.
Taiebat, M. & Dafalias, Y. F. (2008). SANISAND: simple anisotropic sand plasticity model. *Int. J. Numer. Analyt. Methods Geomech.* **32**, No. 8, 915–948.
Taiebat, M., Jeremić, B., Dafalias, Y. F., Kaynia, A. M. & Cheng, Z. (2010). Propagation of seismic waves through liquefied soils. *Soil Dyn. Earthq. Engng* **30**, No. 4, 236–257.
Ueda, K., Vargas, R. R. & Uemura, K. (2018). LEAP-Asia-2018: stress–strain response of Ottawa sand in cyclic torsional shear tests. *DesignSafe-CI*, https://doi.org/10.17603/DS2D40H.
Vaid, Y. P., Stedman, J. D. & Sivathayalan, S. (2001). Confining stress and static shear effects in cyclic liquefaction. *Can. Geotech. J.* **38**, No. 3, 580–591.
Wang, Z. L., Dafalias, Y. F. & Shen, C. K. (1990). Bounding surface hypoplasticity model for sand. *J. Engng Mech.* **116**, No. 5, 983–1001.
Wang, R., Zhang, J. M. & Wang, G. (2014). A unified plasticity model for large post-liquefaction shear deformation of sand. *Comput. Geotech.* **59**, 54–66.
Wichtmann, T. & Triantafyllidis, T. (2016). An experimental database for the development, calibration and verification of constitutive models for sand with focus to cyclic loading: part I – tests with monotonic loading and stress cycles. *Acta Geotech.* **11**, No. 4, 739–761.
Woo, S., Salgado, R. & Prezzi, M. (2019). Dilatancy-triggering surface for advanced constitutive modelling of sand. *Géotechnique Lett.* **9**, No. 2, 136–141, https://doi.org/10.1680/jgele.17.00085.
Yang, J. & Sze, H. Y. (2011). Cyclic behaviour and resistance of saturated sand under non-symmetrical loading conditions. *Géotechnique* **61**, No. 1, 59–73, https://doi.org/10.1680/geot.9.P.019.
Yang, M., Seidalinov, G. & Taiebat, M. (2019). Multidirectional cyclic shearing of clays and sands: evaluation of two bounding surface plasticity models. *Soil Dyn. Earthq. Engng* **124**, 230–258.
Yoshimine, M., Ishihara, K. & Vargas, W. (1998). Effects of principal stress direction and intermediate principal stress on drained shear behavior of sand. *Soils Found.* **38**, No. 3, 177–186.
Zhang, J. M. & Wang, G. (2012). Large post-liquefaction deformation of sand, part I: physical mechanism, constitutive description and numerical algorithm. *Acta Geotech.* **7**, No. 2, 69–113.